Struct Multidisc Optim (2016) 53:673–694
DOI 10.1007/s00158-015-1309-x

RESEARCH PAPER

Polygonal multiresolution topology optimization (PolyMTOP) for structural dynamics

Evgueni T. Filipov · Junho Chun · Glaucio H. Paulino · Junho Song

Received: 22 July 2013 / Revised: 2 September 2014 / Accepted: 22 October 2014 / Published online: 5 November 2015

Abstract We use versatile polygonal elements along with a multiresolution scheme for topology optimization to achieve computationally efficient and high resolution designs for structural dynamics problems. The multiresolution scheme uses a coarse finite element mesh to perform the analysis, a fine design variable mesh for the optimization and a fine density variable mesh to represent the material distribution. The finite element discretization employs a conforming finite element mesh. The design variable and density discretizations employ either matching or non-matching grids to provide a finer discretization for the density and design variables. Examples are shown for the optimization of structural eigenfrequencies and forced vibration problems.

Evgueni T. Filipov and Junho Chun were equal contribution authors.

Partially presented at 10^{th} World Congress on Structural and Multidisciplinary Optimization, Orlando, FL, May 20-24, 2013.

E. T. Filipov · J. Chun · G. H. Paulino
Department of Civil and Environmental Engineering, University of Illinois at Urbana-Champaign (UIUC), Urbana, IL 61801, USA

E. T. Filipov
e-mail: filipov1@illinois.edu

J. Chun
e-mail: jchun8@illinois.edu

J. Song
Department of Civil and Environmental Engineering, Seoul National University, Seoul, 151-742, Republic of Korea
e-mail: junhosong@snu.ac.kr

G. H. Paulino (✉)
School of Civil and Environmental Engineering, Georgia Institute of Technology, 790 Atlantic Drive, Atlanta, GA 30332, USA
e-mail: paulino@gatech.edu

Keywords Topology optimization · Multiresolution · Polygonal elements · Eigenfrequency optimization · Forced vibration optimization

1 Introduction

In recent times topology optimization has been used in the design of aircraft (Maute and Allen 2004; Sleesongsom and Bureerat 2013), cars (Yang and Chahande 1995), buildings (Mijar et al. 1998; Stromberg et al. 2011), and even human bones (Sutradhar et al. 2010). The use of topology optimization has increased over the past few decades in part due to improving capabilities of computational modeling, but also due to improved understanding of the continuum optimization problem. Recent advances such as the solid isotropic material with penalization (SIMP) material interpolation model (Bendsøe MP 1989; Rozvany et al. 1992) has allowed for effective discretization of continuum domains, and filtering methods (e.g. Sigmund and Petersson 1998; Petersson and Sigmund 1998; Guest 2004; Almeida et al. 2009) have allowed for mesh independent solutions.

Structural dynamic modeling has similarly evolved in the past years and can include modal, time history, or transformed problem analysis. Topology optimization for freely vibrating systems has included the design of beams, trusses, plates and other systems (Olhoff 1976; Du and Olhoff 2007; Olhoff et al. 2012; Zhou 2013). Typically these systems are designed such that the natural frequencies of the structure are changed from the initial configuration. Recent research (Yoon 2010a, b; Huang et al. 2010) has introduced dynamic optimization for nonlinear structures. Alternatively, Tsai and Cheng (2013) have developed a method for optimizing dynamic structures and fixing a

specific mode shape. Optimization can also be performed for forced vibration systems where a system is designed such that the maximum response (dynamic displacement) for a given input frequency is optimized. Recent research has shown that the structural response for resonating structures can be maximized (Tcherniak 2002) or, more typically, minimized (Ma et al. 1995; Jog 2002; Dahl et al. 2007; Jensen 2007; Larsen et al. 2008) for a set of design frequencies.

Recent advances in finite element (FE) modeling (e.g. Sukumar 2004; Sukumar and Malsch 2006; Ghosh 2011) have allowed for the use of polygonal elements in continuum modeling. A significant benefit of these elements is that they are well suited for modeling of complex domains and can be used to easily create areas of high and low mesh refinement. In topology optimization these elements have been shown to significantly reduce instabilities associated with checkerboard and islanding effects, and have been shown to be stable and accurate (Jog and Haber 1996; Talischi et al. 2009a, b). Recent educational codes (Talischi et al. 2012a, b) provide a polygonal element mesher and a package for efficient topology optimization, and these codes are used as the basis for the work presented herein. Furthermore, recent advances in multiresolution modeling have allowed for high resolution results with relatively low computational costs. Nguyen et al. (2009, 2012), introduce Multiresolution Topology Optimization (MTOP), and use different overlying meshes for FE analysis and for the density/design variables, to harvest the higher order accuracy of the displacement solution in obtaining higher resolution solutions. Such mesh refinements and adaptivity techniques can provide significant improvements in computational speed and solution resolution. Other methods have taken advantage of higher-order finite elements to improve the speed and quality of topology optimization. For example Parvizian et al. (2011) use a finite cell method to separate geometry and FE analysis, while Nguyen et al. (2013) use high-order elements to enhance the MTOP approach.

In this paper, we adapt the existing polygonal finite element codes (Talischi et al. 2012a, b), with higher resolution density and design discretizations to obtain high fidelity multiresolution designs (Nguyen et al. 2009) for structural dynamic problems. This combined modeling approach (PolyMTOP), provides adaptable, high resolution structural optimization techniques that can be used to tailor the dynamic performance of buildings, vehicles and other systems. This paper is organized as follows: Section 2 provides an overview of the multiresolution approach and introduces the formulation for matching and non-matching multiresolution discretizations; Section 3 presents the topology optimization framework used for static and dynamic problems; Section 4 explains the numerical implementation; Section 5 shows the approach used in the optimization of static compliance problems; Section 6 provides examples of eigenfrequency optimization; Section 7 discusses examples of forced vibration problems; and Section 8 presents concluding remarks.

2 Multiresolution approach for polygonal elements

2.1 Matching and non-matching sub-discretizations

In the multiresolution approach, the *design variables* in the optimization framework are material densities for a predefined portion of the mesh. Subsequently, a projection filter (Section 3.4) is used to obtain a mesh independent solution of *density variables* that are used to represent the actual material distribution and to compute stiffness and mass matrices. There are various ways in which the design variable can be positioned such that it does not overlap with the FE mesh, for example, nodal approaches (Guest et al. 2004; Rahmatalla and Swan 2004; Matsui and Terada 2004) use design variables that are placed on individual nodes, or alternatively design variables can be placed between nodes such as in Paulino and Le (2008). Alternatively, the multiresolution scheme introduced in Nguyen et al. (2009) uses coarser meshes for FE analysis and finer mesh discretizations for optimization and design. This generates a high-resolution result without a significant increase in computational cost. Furthermore, the same authors showed that by using alternative design and density variable placement, and an adaptive multiresolution approach they could obtain higher efficiency (Nguyen et al. 2012). Expanding the multiresolution approach to polygonal elements, there are various ways in which a polygonal element can be divided such that the design mesh is finer than the FE mesh. In this paper, several cases are considered where elements are divided in matching and non-matching sub-discretizations, however, in all cases, the design variables are at the same location as the density variables. For example, Fig. 1 shows the superposition of design, and density variables with a matching method for a five sided polygonal element.

For matching sub-discretizations, the element is first divided into triangular slices from the centroid (thick gray lines in Fig. 2a and b), and each slice is subsequently divided into three (M3 approach) or four (M4 approach) equivalent pieces. For non-matching sub-discretizations, the finite element is divided into convex, Centroidal Voronoi Tessellations (CVTs). Figure 2a shows the matching, M3 approach, where the naming *P5/M3/n15* is used to indicate: a five sided polygon/with matching sub-discretization

M3/resulting in 15 design variables for the element. Similarly, the non-matching elements in Fig. 2d and e can be named as P5/n7 and P5/n18 respectively, indicating the number of edges of the polygon and the number of design variables placed inside. Both approaches can easily be applied to any type of polygon in the FE mesh.

The matching approach ensures that the number of design and density variables will be proportional to the number of nodes of the element and there will be continuity between the variables of different elements, however the influence area of each variable could be different. The non-convex approach on the other hand, uses the same number of sub-discretizations based on randomly placed seeds within each element. As shown in Fig. 3, these seeds are moved using a Lloyd algorithm to create CVTs that consist of regularized convex elements (Talischi et al. 2009b). Note that the Lloyd algorithm allows the sub-discretizations to be relatively uniform with similar areas within each element.

2.2 Stiffness and mass matrix computing

For a discretized finite element mesh, the global stiffness matrix can be calculated as:

$$\mathbf{K} = \sum_{e=1}^{N_{el}} \mathbf{K}_e = \sum_{e=1}^{N_{el}} \int_{\Omega_e} \mathbf{B}^{\mathrm{T}} \mathbf{D} \mathbf{B} d\Omega \tag{1}$$

where N_{el} are the number of elements, $\mathbf{B}$ is the strain-displacement matrix of shape function derivatives, and $\mathbf{D}$ is the constitutive matrix. The constitutive matrix is calculated for a plane stress case (Cook et al. 2007) and the Young's modulus is calculated as a function of the density ρ at position $\mathbf{x}$ on the multiresolution mesh, as

$$E(\mathbf{x}) = \rho(\mathbf{x})^p E^0 \tag{2}$$

In (2), E^0 is the Young's modulus of solid material and the objective in topology optimization is to determine the distribution of material in the domain to satisfy a set of

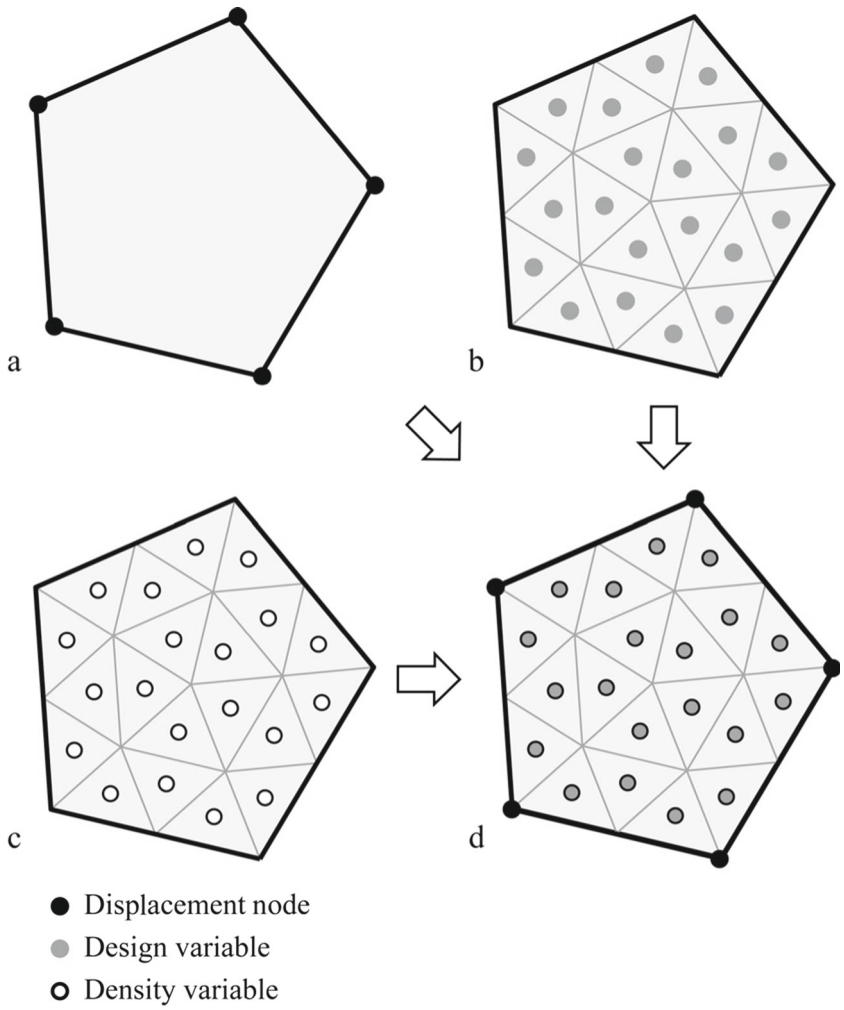

Fig. 1 Five sided polygon element with M4 design variable mesh: **a** Finite element (displacement based), **b** Design variable mesh, **c** Density variable mesh, **d** Superposed meshes

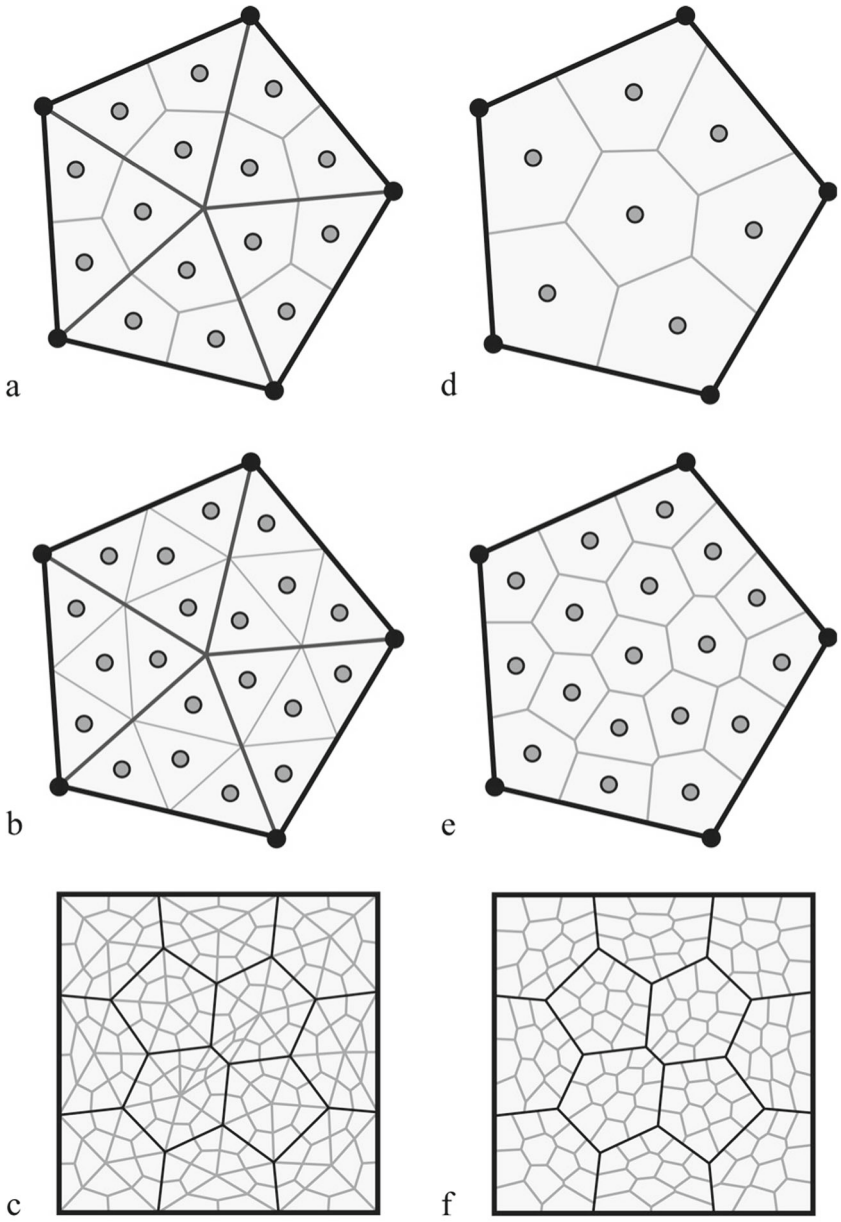

Fig. 2 Sub-discretizations for five sided polygon element: **a** P5/M3/n15, **b** P5/M4/n20, **c** Mesh of Pn/M3 matching elements, **d** P5/n7, **e** P5/n18, **f** Mesh of Pn/n12 non-matching elements

objectives. To achieve this, a SIMP model is used to penalize locations of intermediate densities. The value of the density $\rho(\mathbf{x})$ can be between $\rho_{min} = 10^{-3}$ and 1, and the penalization parameter p is chosen to be more than 1 (typically 3 or 4) and can be used in an incremental iterative fashion. This type of model serves to transform the discrete formulation into a continuous solvable problem that can be treated numerically. Since the stiffness matrix is linearly dependent on the elastic modulus, the penalized density terms $(\rho(\mathbf{x})^p)$ are taken out from the integration of the stiffness matrix, as shown in (3). Within this work, shape functions were integrated at the centroid of each cell of the element as this is sufficiently accurate to calculate the stiffness matrix of each element, and so the element stiffness matrix is approximated as:

$$\mathbf{K}_e \cong \sum_{i=1}^{N_n} (\rho_i)^p \mathbf{B}^{\mathrm{T}} \mathbf{D}^0 \mathbf{B}|_i A_i = \sum_{i=1}^{N_n} (\rho_i)^p \mathbf{I}_i \tag{3}$$

where

$$\mathbf{I}_i = \mathbf{B}^{\mathrm{T}} \mathbf{D}^0 \mathbf{B}|_i A_i, \tag{4}$$

and N_n is the number of integration points on each element, and (ρ_i) represents the density at each integration point.

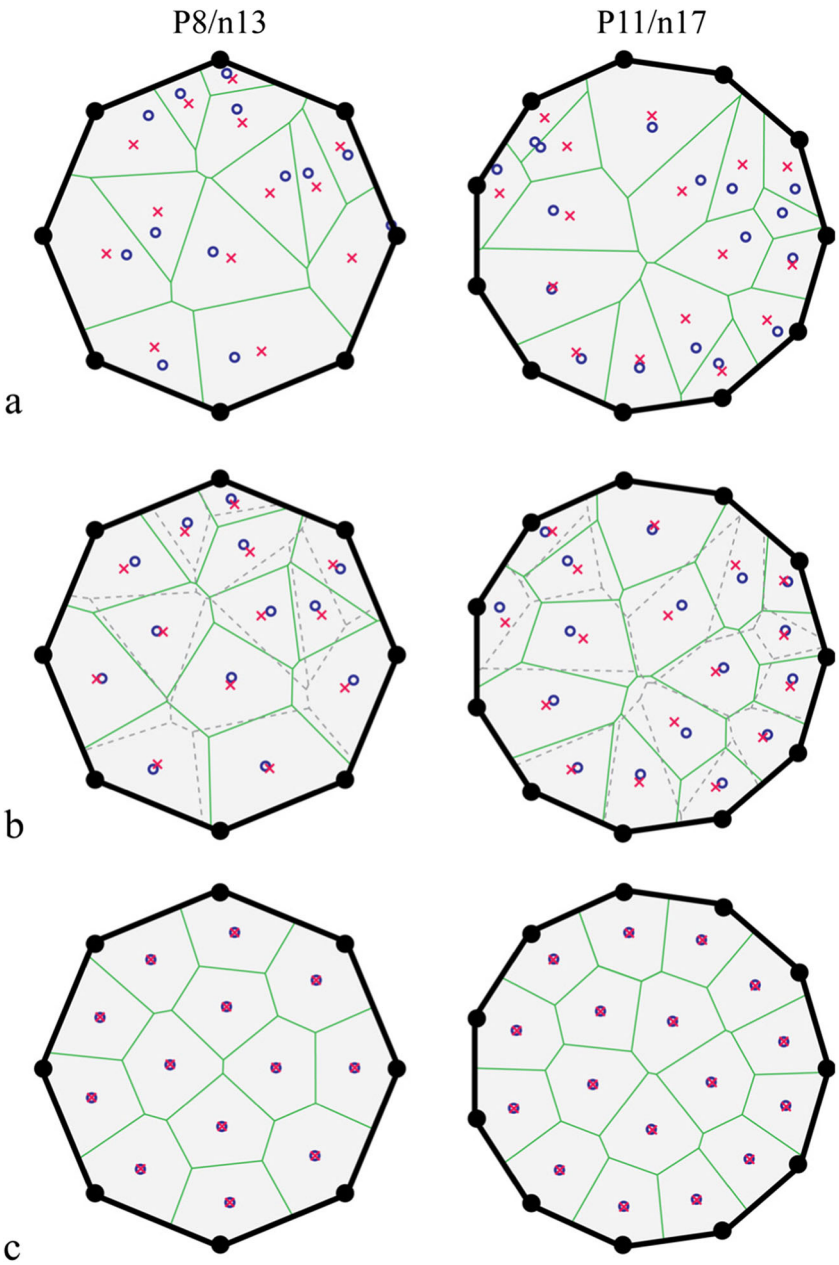

Fig. 3 Illustration of Lloyd's algorithm optimizing the sub-discretizations of a P8/n13, and a P11/n17 element: **a** initial distribution of seeds (*circles*), the corresponding Voronoi diagram, and the centroid of the Voronoi cells (*crosses*), **b** the Voronoi diagram after one iteration, **c** the Voronoi diagram after 50 iterations

The global mass matrix can similarly be calculated by integrating over the domain as:

$$\mathbf{M} = \sum_{e=1}^{N_{el}} \mathbf{M}_e = \sum_{e=1}^{N_{el}} \int_{\Omega_e} \rho \mathbf{N}^{e\mathrm{T}} \mathbf{N}^e d\Omega \tag{5}$$

where N^e denote the element shape functions. The element mass matrix ($\mathbf{M}_e$) can furthermore be approximated by

$$\mathbf{M}_e \cong \sum_{i=1}^{N_n} (\rho_i)^q \mathbf{N}_i^{e\mathrm{T}} \mathbf{N}_i^e|_i A_i = \sum_{i=1}^{N_n} (\rho_i)^q \mathbf{H}_i \tag{6}$$

where q is the penalization factor of density for mass terms, and $\mathbf{H}_i$ is used to store the element mass matrix for each integration point in the multiresolution element, as:

$$\mathbf{H}_i = \mathbf{N}_i^{e\mathrm{T}} \mathbf{N}_i^e|_i A_i \tag{7}$$

2.3 Verification of polygonal elements

Mesh variations with quadrilateral, triangular and general polygonal meshes were tested as shown in Fig. 4a through f. Figure 4g shows the convergence error in estimation of the lowest eigenfrequency (ω_1) of the irregular geometry swept panel studied in Cook et al. (2007) using these meshes. Figure 4h on the other hand, shows the mesh convergence

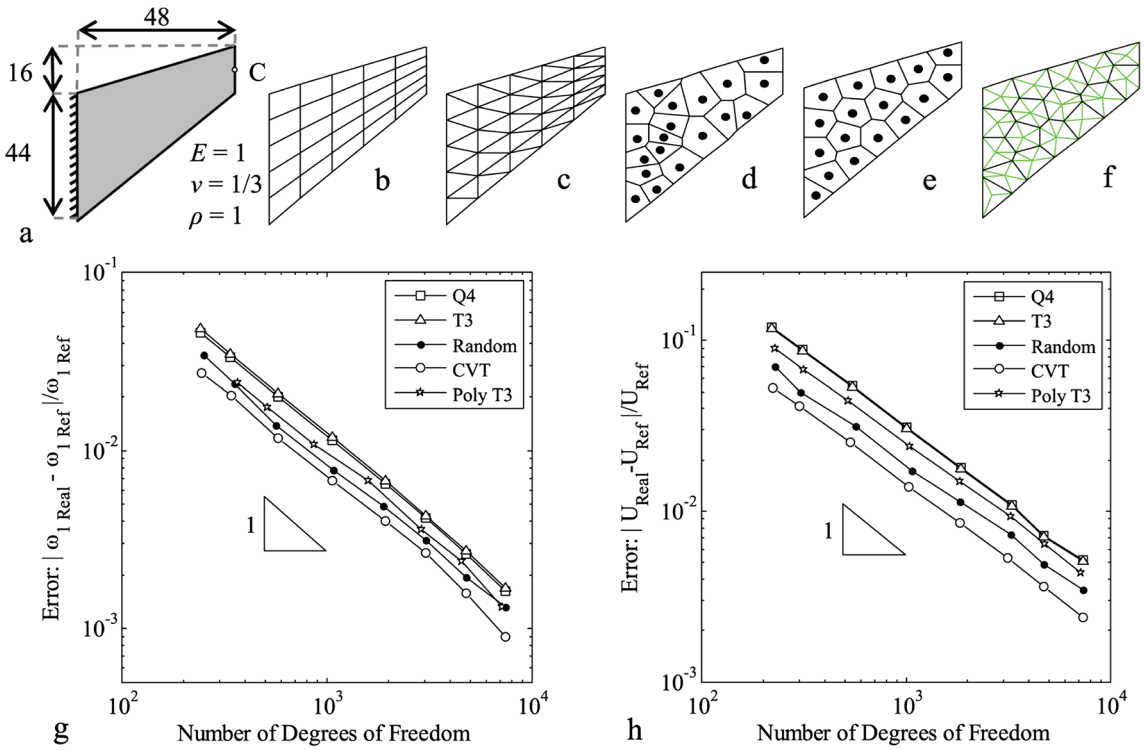

Fig. 4 **a** Geometry, boundary conditions, and properties for Cook's swept panel problem (Cook et al. 2007, p. 108), **b** Quadrilateral (Q4) mesh (25 elements, 36 nodes), **c** Triangular (T3) mesh (50 elements, 36 nodes), **d** Randomized polygonal mesh (19 elements and 36 nodes), **e** Polygonal CVT mesh (17 elements, 36 nodes), **f** Mesh in (e) divided into a mesh of T3 elements (85 elements, 53 nodes), **g** Convergence of minimum eigenfrequency with respect to mesh DOFs, **h** Convergence of steady state solution with respect to mesh DOFs

of the same structure for the obtaining real part of displacements in the steady state solution at point C on Fig. 4a under a harmonic excitation. The excitation is applied on the left edge and its angular frequency is 0.01 rad/s with a force magnitude 1. For the force vibration problem, the Rayleigh damping model, $\mathbf{C} = 0.001\mathbf{M} + 0.001\mathbf{K}$, is used to construct a damping matrix. Because there is no analytical solutions for the two tested problems, solutions were obtained by using a much finer discretization of about 10^5 degrees of freedom (DOFs) to calculate a reference solution. For the same number of DOFs, the polygonal mesh where the Lloyd algorithm was used to refine the mesh (Fig. 4e), provides better approximation for structural dynamic properties. The results of the polygonal mesh are the average errors of five individual simulations. Since a log-log scale is used it can be seen that the polygonal element mesh has better accuracy than the other mesh discretizations.

2.4 Verification of MTOP approach

A patch test inspired by the one presented by Parvizian et al. (2011), for static analysis, was performed to test the performance of PolyMTOP approach in analyzing structures with discrete internal voids. The test shown in Fig. 5a is a 10×10 square with a centrally placed circular void of radius 2.5. The structure is restrained on the bottom edge and a distributed load of 1 is applied on the top edge. Figure 5b through e present several meshes that employ conventional elements as well as MTOP approaches in modeling the structure. Each element or density variable whose centroid is outside of the void area has an elastic modulus (E) of 10^4, while those within the void have $E = 10$. A Poisson's ratio of $\nu = 0.3$ and material density of $\rho = 1$ are used uniformly throughout the mesh. Figure 6 shows the area of the solid material approximated by the different finite element and multiresolution methods with respect to the number of DOFs in the mesh. Note that each approach and each discretization approximates the area differently, so it is possible that a coarse mesh may by an odd chance provide good approximation for the solid area and/or the mechanical behavior of the structure. It is evident that for most discretizations, the MTOP approach performs better in estimating the area than the regular approaches because there are a lot more density variables for the same number of DOFs. Figure 5g shows the error of maximum displacement for the different discretizations, while Fig. 5h shows the error for calculating the minimum eigenfrequency of the structure.

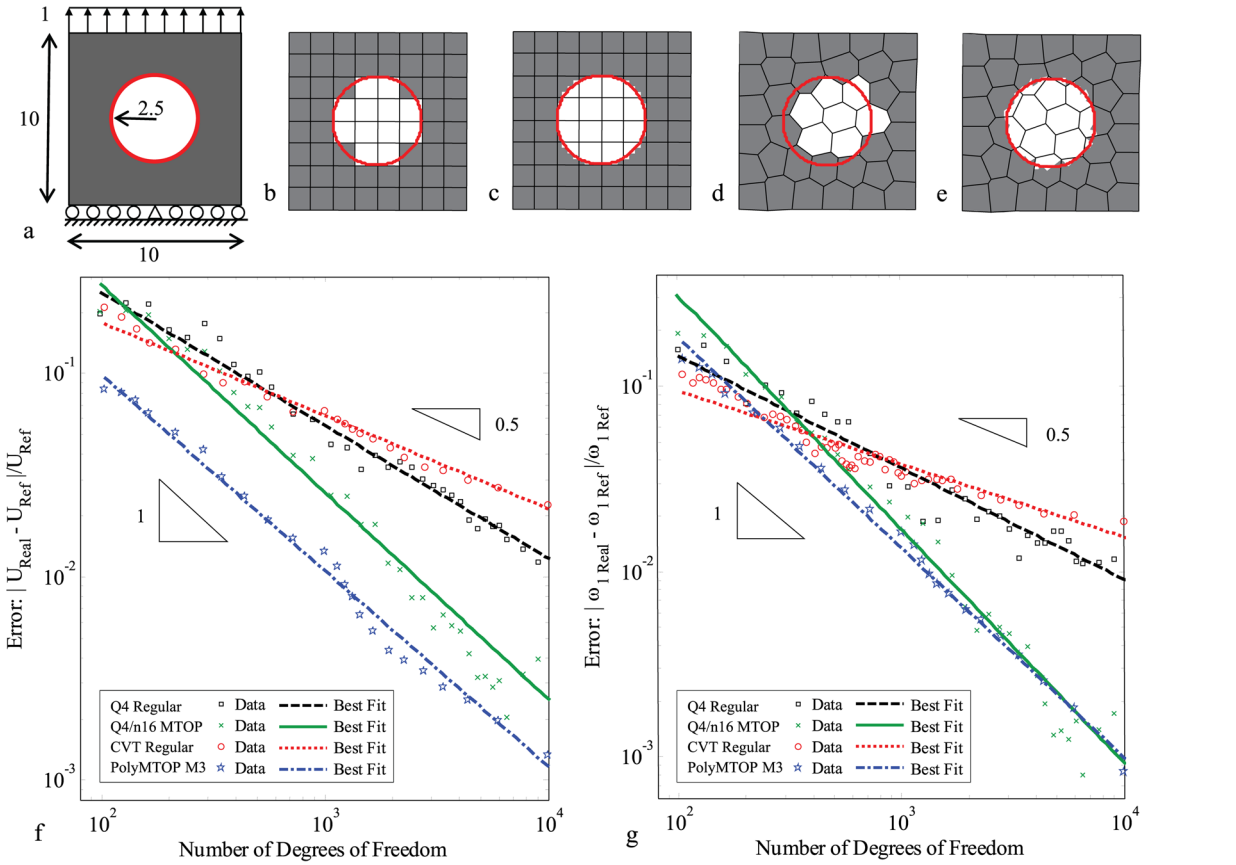

Fig. 5 **a** Geometry, boundary conditions and properties for patch test, **b** Quadrilateral (Q4) mesh (64 elements, 81 nodes), **c** Q4/n16 MTOP mesh (64 elements, 81 nodes, 1024 design variables), **d** CVT polygonal mesh (40 elements and 81 nodes), **e** PolyMTOP M3 mesh (40 elements, 81 nodes, 648 design variables), **f** Error of maximum static displacement with respect to mesh DOFs, and **g** Error of minimum eigenfrequency with respect to mesh DOFs (Note that not all data points are shown for clarity)

The reference solution against which the error is calculated is obtained by discretizing the problem with a much finer mesh ($\approx 10^5$ DOFs). Because some meshes may overestimate, while others may underestimate the FE results, there is substantial scatter in the original data, and for that reason each of the polygonal data points is an average of 5 separate analyses for different random meshes. Furthermore, to alleviate the scatter, unweighted smoothing is applied to all data, and each data point is replaced with the average of the 5 adjacent points (i.e. the data point, 2 points with lower and 2 points with higher DOFs). A best fit line is subsequently placed for each of the cases. The MTOP approaches converge at a higher rate than the conventional Q4 and Polygonal CVT meshes. Note that, when a polygonal mesh is used, there are much fewer elements and design variables for the same number of DOFs (e.g. see Fig. 5), and thus one might expect that it would be more difficult to model the void in the structure. However, the regular Polygonal mesh performs roughly as well as a regular Q4 mesh for the range of discretizations studied, while the PolyMTOP scheme performs with about the same or with higher accuracy than the Q4 MTOP analysis for the same number of DOFs.

3 Topology optimization

3.1 Static compliance

A typical objective used for static optimization is the minimization of compliance, which provides the stiffest structure for a defined set of loads, and uses a constraint on the volume on the structure. The continuum problem is typically solved using finite elements and can be written in discrete form as:

$$\min_{\rho} \; C(\rho, \mathbf{u}) = \mathbf{f}^{\mathrm{T}}\mathbf{u} \tag{8}$$

$$\text{s.t.} \quad V(\rho) = \int_{\Omega} \rho dV \leq V_s \tag{9}$$

where $\mathbf{f}$ and $\mathbf{u}$ are the global force and displacement vectors, V is the volume as a function of the densities, and V_s is

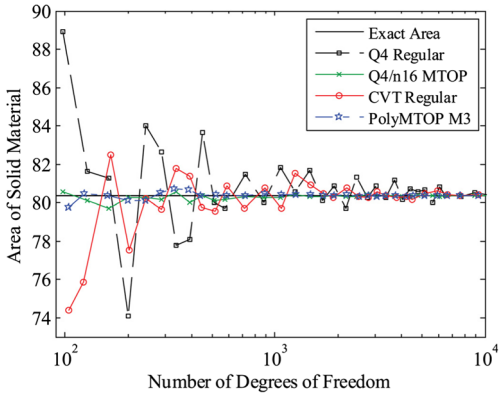

Fig. 6 The area of the solid material in Fig. 5a when approximated by different methods

the prescribed volume fraction. In the above equation, the density is calculated as a function of the design variables $\mathbf{d}$, ($\rho = f(\mathbf{d})$), and the displacement is calculated from the linear equation below:

$$\mathbf{K}(\rho)\mathbf{u} = \mathbf{f} \tag{10}$$

3.2 Eigenfrequency optimization

For dynamics, the linear system of equations can be used to solve the underlining eigenvalue problem. The objective function for free vibration problems can typically be written as a max - min problem in the following form:

$$\begin{aligned} &\max_{\rho} \left\{ \lambda_{min} = \min_{i=1,...,Ndof} \{\omega_j^2\} \right\} \\ &\text{s.t.} \quad V(\rho) = \textstyle\int_\Omega \rho dV = V_s \end{aligned} \tag{11}$$

In the above equations, λ_j is the j^{th} eigenvalue of the free vibrating structure, such that ω_j is the jth eigenfrequency, and ϕ_j is the corresponding eigenvector. The above structural optimization problem uses eigenfrequency behavior based on:

$$\phi_j^{\mathrm{T}} \mathbf{M} \phi_k = \delta_{jk}, \quad j \geq k, \quad k, j = 1, ..., N_{dof} \tag{12}$$

$$\mathbf{K}\phi_j = \omega_j^2 \mathbf{M}\phi_j, \quad j = 1, ..., N_{dof} \tag{13}$$

where δ_{jk} is the Kronecker's delta. The stiffness and mass matrices are symmetric and positive definite and the eigenfrequencies considered are real. The eigenfrequencies can be sorted in order of magnitude as: $0 < \omega_1 \leq \omega_2 \leq ... \leq \omega_{N_{dof}}$. In eigenvalue problems, it is often the case that multiple eigenvalues may be encountered. This could be due to symmetries in the structure, or due to the optimization procedure which could lead to physically different eigenmodes, to give the same eigenfrequency value. This problem is relatively well understood and has been addressed, for example, by Bratus and Seiranian (1983), Masur (1985), and Seyranian et al. (1994), among others. A typical method for overcoming this problem is using a bound formulation (Bendsøe et al. 1983; Taylor and Bendsøe 1984; Olhoff 1989) where a scalar variable β is used in the objective function to envelope multiple eigenfrequencies and to serve as a lower bound for the objective function. This approach can also be used with multiple βs to maximize multiple eigenfrequencies or to create a band-gap in the structural response:

$$\begin{aligned} &\max_{\rho,\beta_1,\beta_2} \{\beta_2 - \beta_1\} \\ &\text{s.t.} \quad \beta_2 - \omega_j^2 \leq 0, \qquad j = n, n+1, ..., J \\ &\qquad \omega_j^2 - \beta_1 \leq 0, \qquad j = 1, ..., n-1 \\ &\qquad V(\rho) = \int_\Omega \rho dV = V_s \end{aligned} \tag{14}$$

Note that constraints for volume, and the dynamic characteristics from the previous equations are still valid here, and note also that if the second inequality was removed and the bound was set to the first eigenfrequency then this would give the same results as the fundamental frequency case. During the optimization process, it is also possible to encounter spurious eigen modes in locations where there is a low amount of material since the penalization factors p and q cause for a local mass that is much larger relative to the simulated stiffness. To avoid these modes, an approach suggested by Tcherniak (2002), and Du and Olhoff (2007) is used, and the mass penalization parameter q is set artificially high ($q = 6$) in locations where the density $\rho < 0.1$. This modification eliminates localized modes from interfering with the optimization, but has a negligible effect overall since the modified areas have little influence on the eigen modes of interest.

3.3 Forced vibrations

3.3.1 Equation of motion

Forced harmonic vibrations are of importance to practical mechanisms and are often encountered in engineering systems. The equation of motion of a linear dynamic system in a discretized form is:

$$\mathbf{M}\ddot{\mathbf{u}}(t) + \mathbf{C}\dot{\mathbf{u}}(t) + \mathbf{K}\mathbf{u}(t) = \mathbf{f}(t) \tag{15}$$

where $\ddot{\mathbf{u}}(t)$, $\dot{\mathbf{u}}(t)$ and $\mathbf{u}(t)$ are acceleration, velocity, displacement vectors at time t, respectively. $\mathbf{M}$, $\mathbf{C}$, $\mathbf{K}$ denote mass, damping, and stiffness matrices, and $\mathbf{f}(t)$ is the loading vector as a function of time. It is noted that the system matrices are dependent on a set of design variables $\mathbf{d}$. We assume that the system is subjected to time-harmonic excitations.

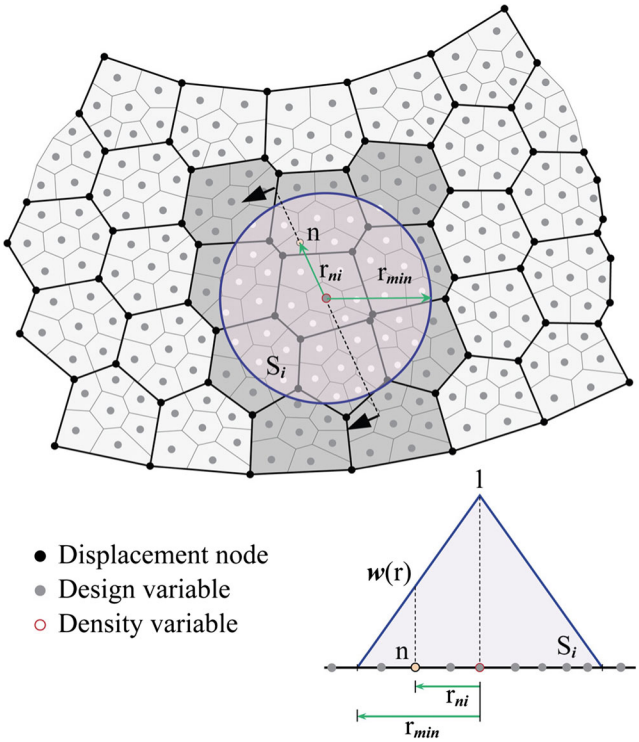

Fig. 7 Projection scheme from the design variables to the density variable

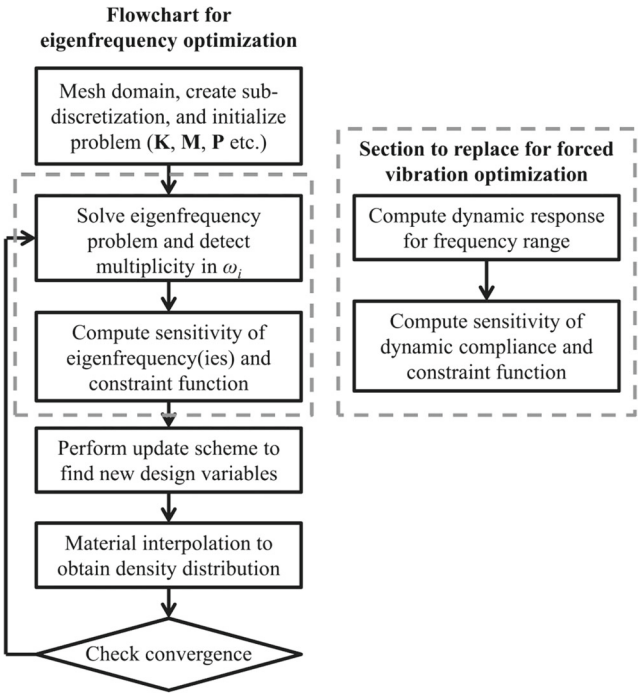

Fig. 8 Numerical implementation for eigenfrequency and forced vibration problems

Thus, the excitations and displacements can be described by the following forms

$$\begin{aligned}\mathbf{f}(t) &= \mathbf{F}_{\mathrm{R}}\cos(\omega t) - \mathbf{F}_{\mathrm{I}}\sin(\omega t)\\ \mathbf{u}(t) &= \mathbf{U}_{\mathrm{R}}\cos(\omega t) - \mathbf{U}_{\mathrm{I}}\sin(\omega t)\end{aligned} \tag{16}$$

where $\mathbf{F}_{\mathrm{R}}$ and $\mathbf{F}_{\mathrm{I}}$ are the vector of the excitation force amplitude, $\mathbf{U}_{\mathrm{R}}$ and $\mathbf{U}_{\mathrm{I}}$ denote the vector of the displacement amplitude. ω is the forcing frequency. The substitution of (16) into (15) yields the following equation

$$\begin{aligned}&\omega^2\mathbf{M}[-\mathbf{U}_{\mathrm{R}}\cos(\omega t) + \mathbf{U}_{\mathrm{I}}\sin(\omega t)]\\ &+\omega\mathbf{C}[-\mathbf{U}_{\mathrm{R}}\sin(\omega t) - \mathbf{U}_{\mathrm{I}}\cos(\omega t)]\\ &\quad+\mathbf{K}[\mathbf{U}_{\mathrm{R}}\cos(\omega t) - \mathbf{U}_{\mathrm{I}}\sin(\omega t)]\\ &\quad= \mathbf{F}_{\mathrm{R}}\cos(\omega t) - \mathbf{F}_{\mathrm{I}}\sin(\omega t)\end{aligned} \tag{17}$$

After arranging coefficients of $\cos(\omega t)$ and $\sin(\omega t)$, equality condition can be held for all time t as following in a matrix form

$$\begin{bmatrix}\mathbf{K}-\omega^2\mathbf{M} & -\omega\mathbf{C}\\ \omega\mathbf{C} & \mathbf{K}-\omega^2\mathbf{M}\end{bmatrix}\begin{pmatrix}\mathbf{U}_{\mathrm{R}}\\ \mathbf{U}_{\mathrm{I}}\end{pmatrix} = \begin{pmatrix}\mathbf{F}_{\mathrm{R}}\\ \mathbf{F}_{\mathrm{I}}\end{pmatrix} \tag{18}$$

Herein, we introduce two complex vectors such as

$$\mathbf{U} = \mathbf{U}_{\mathrm{R}} + i\mathbf{U}_{\mathrm{I}},\ \mathbf{F} = \mathbf{F}_{\mathrm{R}} + i\mathbf{F}_{\mathrm{I}},\ i \in \mathbb{C}(\mathrm{e.g.}i^2 = -1) \tag{19}$$

The real parts of $\mathbf{U}$ and $\mathbf{F}$ are denoted by Re($\mathbf{U}$) and Re($\mathbf{F}$), and the imaginary parts of $\mathbf{U}$ and $\mathbf{F}$ are denoted by Im($\mathbf{U}$) and Im($\mathbf{F}$). With the complex vector, (17) can be expressed in a compact form of complex linear algebraic equations.

$$[\mathbf{K} + i\omega\mathbf{C} - \omega^2\mathbf{M}]\mathbf{U} = \mathbf{F} \tag{20}$$

where the dynamic stiffness matrix $\mathbf{S}$ is defined as

$$\mathbf{S} = \mathbf{K} + i\omega\mathbf{C} - \omega^2\mathbf{M} \tag{21}$$

and thus

$$\mathbf{S}\mathbf{U} = \mathbf{F} \tag{22}$$

The complex displacement $\mathbf{U}$ in (20) can be directly solved by a complex matrix solver. Alternatively, Yoon (2010a) implemented the model reduction scheme which can reduce computational resources to solve the complex system equation of (20).

3.3.2 Dynamic compliance

The steady-state response of the system under harmonic excitations was considered in the frequency domain to

define dynamic compliance (Ma et al. 1995; Jog 2002; Jensen 2007). The dynamic compliance can be expressed as

$$\Phi(\rho, \mathbf{U}_R(\rho), \mathbf{U}_I(\rho)) = \int_{\omega_s}^{\omega_e} |\mathbf{F}^T \mathbf{U}(\rho)| d\omega \quad (23)$$
$$= \int_{\omega_s}^{\omega_e} \sqrt{(\mathbf{F}_R{}^T \mathbf{U}_R - \mathbf{F}_I{}^T \mathbf{U}_I)^2 + (\mathbf{F}_R{}^T \mathbf{U}_I + \mathbf{F}_I{}^T \mathbf{U}_R)^2} d\omega$$

where ω_s, ω_e denote the initial and final angular frequency of the external forces, respectively (i.e. the range of frequencies used in the optimization). The problem statement of the dynamic compliance optimization with the volume constraint V_s can be described as

$$\min_{\rho} \ \Phi(\rho, \mathbf{U}_R(\rho), \mathbf{U}_I(\rho)) = \int_{\omega_s}^{\omega_e} |\mathbf{F}^T \mathbf{U}(\rho)| d\omega$$
$$\text{s.t.} \ \ V(\rho) = \int_{\Omega} \rho dV \leq V_s \quad (24)$$

where the dynamic system satisfies (20).

3.4 Projection scheme

Although the polygonal elements tend to reduce checkerboard and islanding effects in topology optimization, they cannot by themselves provide independence for mesh refinement. Instead, a projection method can be used to achieve a minimum length scale and mesh independence. Previous literature on the subject (Díaz and Sigmund 1995; Sigmund and Petersson 1998; Bourdin 2001; Guest 2009; Wang et al. 2010) provide different approaches on filtering the sensitivities and densities to obtain mesh independent results. Herein we use a previously reported projection method (Guest et al. 2004; Almeida et al. 2009) to filter the density variables. This approach uses a linear function to calculate the density ρ of an element i associated with the surrounding design variable mesh. The density of the element would be computed based on the weighted average of the nearby design variables as

$$\rho_i = \frac{\sum_{n \in S_i} d_n w(x_n - x_i)}{\sum_{n \in S_i} w(x_n - x_i)} \quad (25)$$

where S_i is the sub-domain corresponding to density element i, $\mathbf{x}_n$ is the position of the centroid of the design variable d_n. The weight function for this linear approach can be defined as

$$w(\mathbf{x}_n - \mathbf{x}_i) = \begin{cases} \dfrac{r_{min} - r_{ni}}{r_{min}} & \text{if } r_{ni} \leq r_{min} \\ 0 & \text{otherwise} \end{cases} \quad (26)$$

where r_{ni} is the distance between the centroid of the density element i and the design variable d_n, and r_{min} is a user defined variable that defines the length scale of the filter. The sensitivities of the element density with respect to the design variables are obtained as:

$$\frac{\partial \rho_i}{\partial d_n} = \frac{w(\mathbf{x}_n - \mathbf{x}_i)}{\sum_{m \in S_i} w(\mathbf{x}_m - \mathbf{x}_i)} \quad (27)$$

Finally, the projection is written in matrix form $\mathbf{P}$ as:

$$\mathbf{y} = \mathbf{P}\mathbf{d} \quad (28)$$

where $\mathbf{y}$ is a vector of the filtered densities. As such the projection needs to be calculated only once, in the beginning of the algorithm, whether a linear (above) or nonlinear projection is used. Figure 7 shows a graphical representation of the filtering scheme.

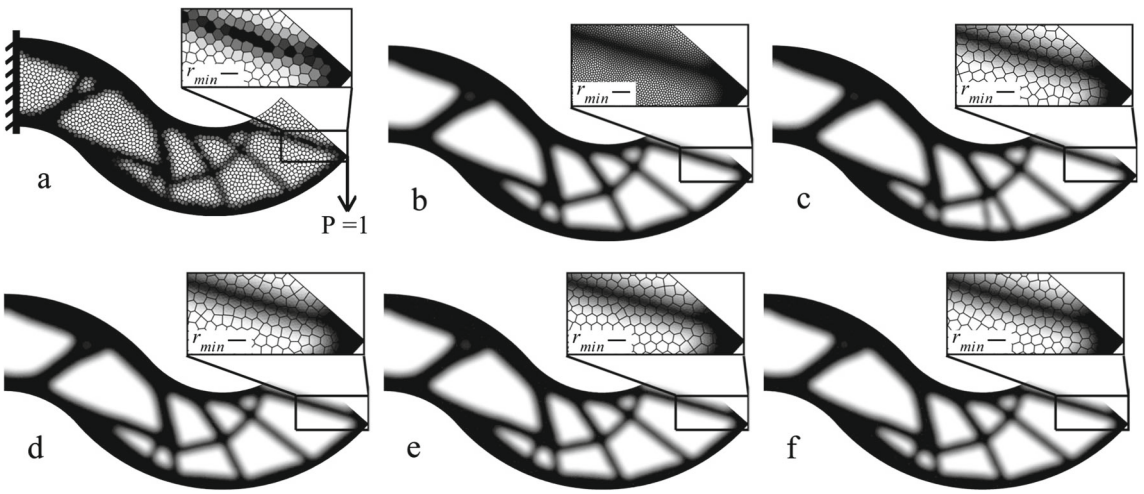

Fig. 9 Static optimization of serpentine domain (Talischi et al. 2012b): **a** Boundary conditions and solution with 2000 n-gons; **b** 40000 n-gons; **c** M3 approach, 2000 n-gons, 35181 design variables; **d** M4 approach, 2000 n-gons, 46912 design variables; **e** Pn/n18 approach, 2000 n-gons, 36000 design variables; **f** Pn/n24 approach, 2000 n-gons, 48000 design variables

Table 1 Computational time for static optimization using regular and PolyMTOP approaches

Discretization	Elements	Nodes	Design/Density variables	Initialization times (seconds)		Optimization time (seconds)		Total time	Static compliance
				PolyMesher	**K** & **M** Calc.	FE Analysis	Optimization		
Coarse polygonal	2000	3975.0	2000	5.77	1.40	16.60	2.99	26.75	415.39
Fine polygonal	40000	79306.8	40000	112.32	33.77	662.78	97.18	906.05	421.94
PolyMTOP M3 Approach	2000	3974.8	35209.8	26.31	4.33	45.62	75.77	152.02	415.84
PolyMTOP M4 Approach	2000	3975.0	46919.2	40.10	5.13	61.10	113.82	220.15	416.02
PolyMTOP /n 18 elements	2000	3982.2	36000	28.87	4.85	46.18	88.82	168.73	415.43
PolyMTOP /n 24 elements	2000	3984.0	48000	43.45	6.47	62.12	125.94	237.99	415.88

4 Numerical implementation

The educational codes published by Talischi et al. (2009a, b) were used as a starting point for this work. The flowchart in Fig. 8 shows the general layout of the algorithm for the eigenvalue optimization with an alternative insert for the forced vibration optimization. In both procedures, polygonal meshing is performed using the PolyMesher software, and matching and non-matching element sub-discretizations are defined. Subsequently, shape functions, mass, stiffness, and projection matrices are calculated and stored to be used later in the optimization procedure. At this point the algorithm enters the optimization loop, and either an eigenfrequency or a forced vibration optimization can be performed. In the first case, the eigenfrequency problem is solved, multiplicity of the eigenfrequencies is detected, and sensitivities are calculated for the eigenfrequencies and constraint functions. We assume that multiplicity in the eigenvalues occurs when the difference between two or more eigenvalues becomes less than 1 % and the sensitivity calculation is then appropriately updated. In the forced vibration case, the dynamic compliance is calculated for the required range of frequencies, and the sensitivities are again appropriately calculated. For an in-depth discussion of the sensitivity calculations the reader is referred to the Appendix of this paper. In both scenarios, the sensitivities are used within an update scheme to calculate a set of new design variables, and the material interpolation function is used to determine the distribution of material density. Finally, the convergence is checked based on the total change in the material distribution at the end of the iteration step, and the algorithm is continued until a tolerance threshold of 1 % is reached.

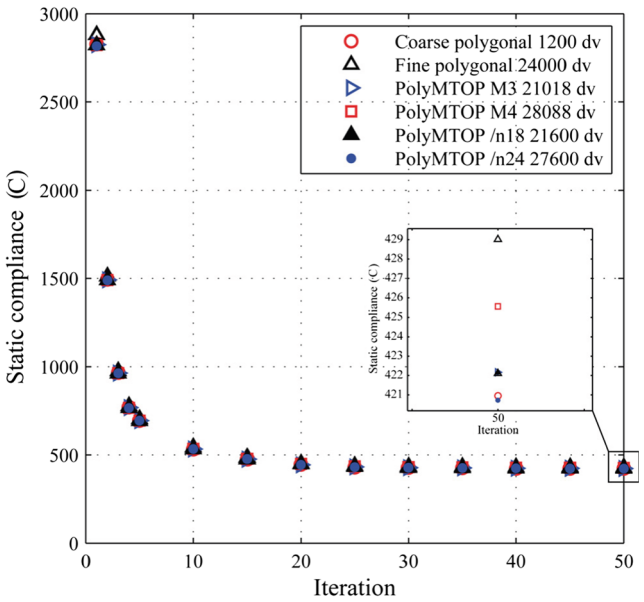

Fig. 10 Convergence history for static compliance minimization of serpentine domain (dv = design/density variables)

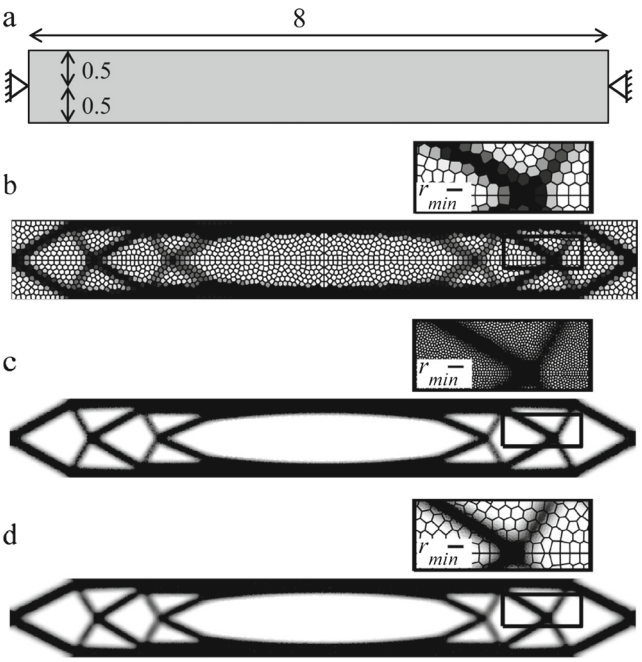

Fig. 11 Optimization of the 1st eigenfrequency of a simply supported beam: **a** Geometry and boundary conditions, **b** Solution with 2000 n-gons, **c** 34000 n-gons, **d** Pn/n17 approach, 2000 n-gons, 34000 design variables

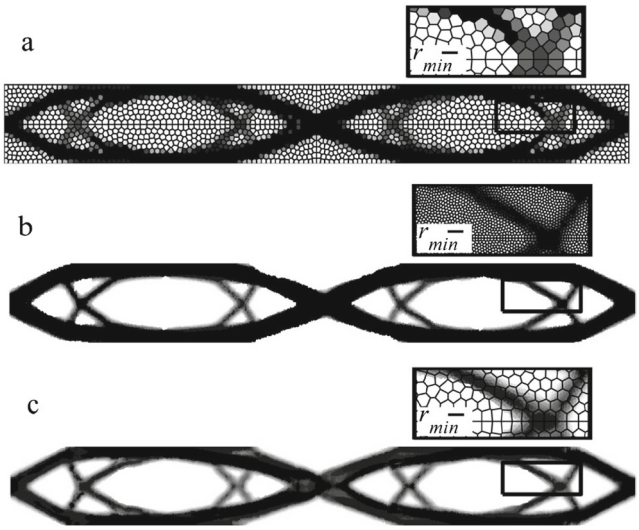

Fig. 12 Optimization of the 2nd eigenfrequency of a simply supported beam: **a** Solution with 2000 n-gons, **b** 34000 n-gons, **c M**3 approach, 2000 n-gons, 34224 design variables

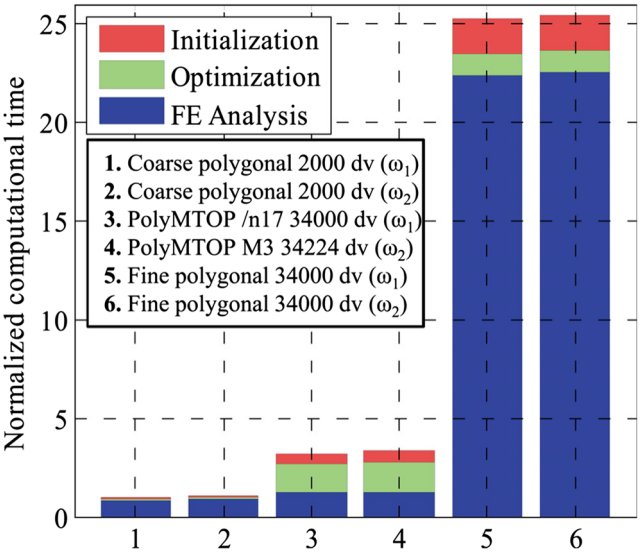

Fig. 13 Comparison of normalized computational times for the optimization of a simply supported beam (dv = design/density variables, ω_1 = optimization for first eigenfrequency, ω_2 = optimization for second eigenfrequency). Times are normalized with respect to the the coarse mesh optimization of ω_1 (60 seconds in this case) and 100 iterations are used for all analyses

5 Static optimization examples

The multiresolution scheme presented above is applied to the serpentine domain presented in Talischi et al. (2012b) (Fig. 9), with a Young's modulus $E = 1$, Poisson's ratio $\nu = 0.3$, and volume fraction V_s set to be at 55 % of the design domain. An optimality criteria based optimizer is used as the update scheme for the design variables, where Lagrangian multipliers control the upper and lower bounds, and a move limit is used to control the step size (Bendsøe and Sigmund 2004). A minimum length scale parameter of $r_{min} = 0.3$ is used, and a penalty parameter $p = 4$ is used in the SIMP model. The length of the parameter $r_{\min}$ is shown graphically as a black line next to the element mesh in cutouts of Fig. 9 and subsequent figures. The discretization adopted employs 2,000 elements with the regular polygonal code, as well as with variants of the different multiresolution approaches. Finally, a mesh of 40,000 elements is considered with the regular PolyTOP code to compare the solution between the conventional and the PolyMTOP frameworks when a similar number of design variables are used. For a sample mesh of 2,000 elements, the distribution of n-gons was 14 P4, 481 P5, 1262 P6, and 243 P7, and the average diameter of the elements was 0.2. This is a typical element size distribution produced by the PolyMesher software, and there were no elements lower than a P4 or higher than a P7, although the code can use such elements as well. Figure 9 shows the static optimal results for the different meshes, where the multiresolution approaches provide a high resolution solution (Fig. 9c, d, e, f) that is essentially the same as that of the fine finite element case (Fig. 9b). Table 1 shows the averaged parameters and computational time for five analyses of each different case[1] carried out to 200 optimization iterations. The multiresolution approach takes roughly the same time in the FE analysis as the coarse mesh since there are the same number of DOFs in the system, while there is an increase in the initialization time (meshing and initial calculation of the **K** and **M** matrices) and optimization time (calculating gradients and using optimization algorithm). The multiresolution approaches are still about four times faster than the fine conventional polygonal mesh, where most of the additional time is spent in the FE analysis. From Table 1, the meshes with 2,000 elements have roughly the same compliance whereas the fine element discretization has a somewhat higher compliance. This is because the finer mesh can better estimate the displacement field for the same structure. To provide mesh independence this example has a relatively large length scale parameter in comparison to the element diameter, there are smooth transitions in material distribution and we cannot observe the advantage that the PolyMTOP approach has in modeling discrete boundaries (Section 2.4). As noted in Nguyen et al. (2009) the MTOP methods can provide mesh independence even when a small r_{min} is used, and in such cases the MTOP approach could still estimate the displacement field accurately. The convergence history of static compliance for the first 50 steps of individual analyses is shown in Fig. 10. Note that all methods follow the

[1] A modern (2013) quad-core 2.93Ghz Intel Xeon® processor is used for the analyses.

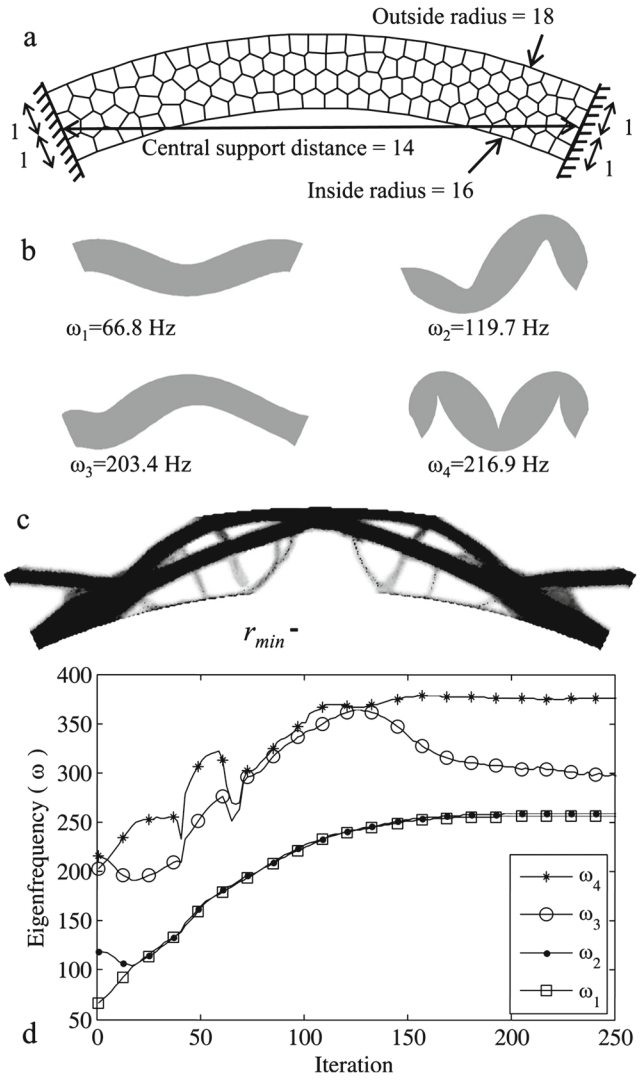

Fig. 14 **a** Geometry and boundary conditions for arch structure (representative mesh only, not used in analysis), **b** Eigen modes and eigenfrequencies of arch before optimization, **c** Structure optimized for mode 1 vibration (maximization of ω_1), **d** Convergence history of eigenfrequencies for maximization of ω_1 of arch structure

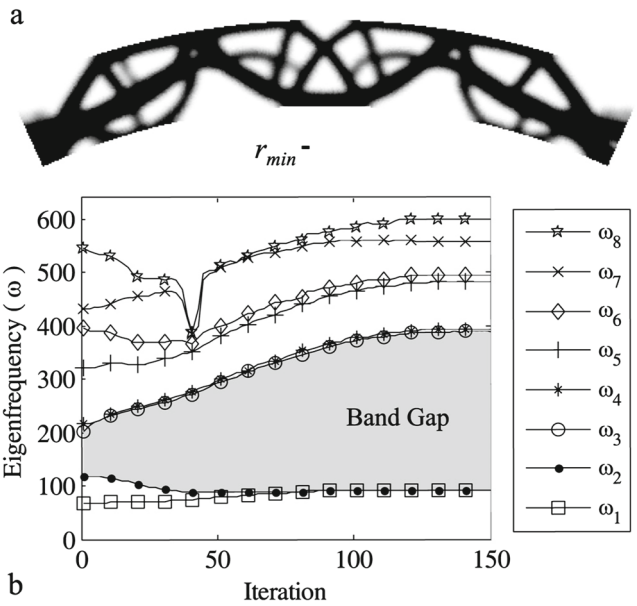

Fig. 15 **a** Structure for maximized ω_3-ω_2 band-gap, **b** Convergence history of eigenfrequencies for maximization of ω_3-ω_2 band-gap of arch structure

same convergence pattern and result in essentially the same optimal compliance (only 1 % difference).

6 Eigenfrequency optimization examples

6.1 Simply supported beam structure

Next, we optimize a simply supported beam of length 8, and a depth of 1, similar to that shown in Du and Olhoff (2007), with a Young's modulus $E = 10^7$, Poisson's ratio $\nu = 0.3$, and volume fraction V_s set to be at 50 % of the design domain. Optimality criteria is used as the optimization algorithm for this and subsequent eigenfrequency problems. A minimum length scale parameter of $r_{min} = 0.09$ is imposed for the beam, and penalization parameters p for stiffness and q for mass, are set to 4 and 1 respectively. The beam is discretized with 2,000 regular polygonal elements, and is optimized for mode 1 vibration (max ω_1) in Fig. 11 and mode 2 vibration (max ω_2) in Fig. 12. Only self mass is imposed on the structure, and no additional masses are suspended in the domain. Results are shown for coarse and fine polygonal meshes, as well as two different multiresolution approaches. Figure 13 depicts the normalized time of each analysis using a bar graph. For this example, the PolyMTOP approach again provides a high resolution solution with computational times being roughly one eighth the time it would take to optimize a conventional mesh with the same order of design and density variables.

6.2 Fixed ends arch structure

An arch structure is also studied for free body vibrations, and again, there is no additional mass placed in the domain. The domain for this structure is shown in Fig. 14a, and 3,000 n-gons with the M4 multiresolution approach (69,120 design variables) are used to produce the examples in Figs. 14c and 15a. For this problem the same properties as the simply supported beam of the previous section are used, except a minimum length scale of $r_{min} = 0.15$ is used. The initial eigenfrequencies are shown for the structure in Fig. 14b, and the methods in Section 3.2 are used to optimize the structure for maximizing the dominant eigenfrequency, as well as for maximizing the band-gap between

the second and third eigenfrequencies. The iteration histories for the optimization are shown in Fig. 14d and 15b. Note that in both cases there are scenarios where multiple eigenfrequencies are encountered by the bound formulation, and the algorithm is capable of effectively fulfilling the objectives. For this structure the eigenfrequency for mode 1 vibration (ω_1) is increased to 221 Hz (Fig. 14d), and the gap between ω_3 and ω_2 is increased by 210 Hz (Fig. 15b). Bandgaps are especially important in structures, since they define a region of frequencies where the structure avoids dynamic resonance. This is a useful property, which can allow for the design of multifunctional structures that can be stiff in some particular situations, but flexible in others.

The validity of the eigenfrequency optimization results may be questioned, since there is a substantial amount of intermediate density (gray material) in the structure, so creating a discrete final design would not ensure that the final optimized eigenfrequency would be obtained. For example, if the structure in Fig. 14c is created into a final design by placing material where $\rho > 0.5$ and removing material where $\rho < 0.5$, then the gray areas would become discontinuous members, and the value of ω_1 would become 261 Hz (18 % increase). To alleviate this issue, it is possible to implement an alternative material interpolation scheme with continuation, or to use a non-linear Heaviside projection to achieve the desired discrete design. For Fig. 16a,

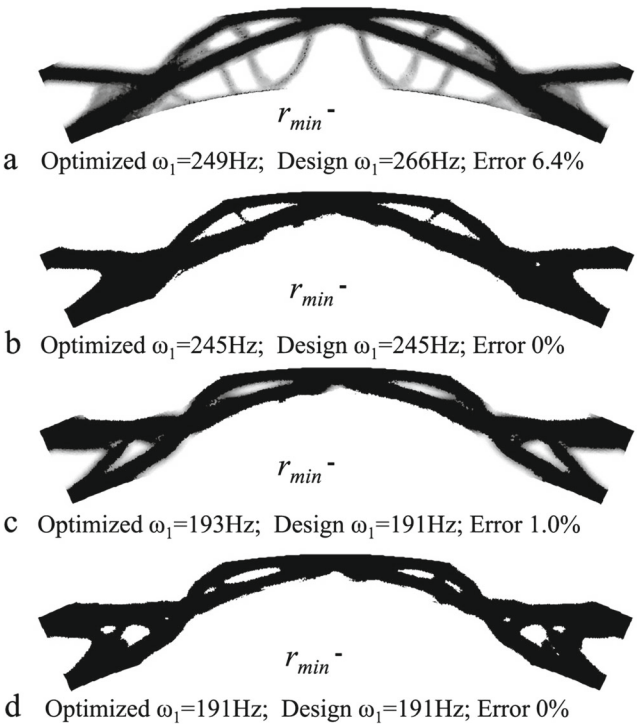

Fig. 16 Arch structure maximization of ω_1 with **a** SIMP continuation, **b** SIMP continuation and Heaviside projection, **c** RAMP continuation, **d** RAMP continuation and Heaviside projection

SIMP penalization was performed with continuation starting with $p = 1$ and being incremented by 0.5 until 4. This provided a small improvement, and reduced the error to 6.4 %. Furthermore, the Rational Approximation of Material Properties (RAMP) scheme (Stolpe and Svanberg 2001) was implemented as:

$$E(\mathbf{x}) = \epsilon + (1-\epsilon)\frac{\rho(\mathbf{x})}{1+s(1-\rho(\mathbf{x}))}, V(\mathbf{x}) = \rho(\mathbf{x}) \quad (29)$$

where the parameter s was set to zero for one step, and continuation was subsequently performed by doubling s from 1 to 64. This approach lead to an even better solution (Fig. 16c) where the error was reduced to about 1 %. Heaviside projection was implemented based on Guest et al. (2004), with the material interpolation functions modified as:

$$E(\mathbf{x}) = \epsilon + (1-\epsilon)[h(\rho(\mathbf{x}))]^p, V(\mathbf{x}) = h(\rho) \quad (30)$$

for SIMP, where

$$h(x) = 1 - \exp(-\beta x) + x\exp(-\beta) \quad (31)$$

In all of the above cases the mass was interpolated linearly per (6) with $q = 1$. In Fig. 16b and c the parameter β in the Heaviside function, was incremented along with the SIMP and RAMP continuation, beginning with $\beta = 0$ for the first step, $\beta = 1$ for the second step, then doubling β every step afterward. The solutions with this approach resulted in essentially black and white solutions where the difference between the initial optimal solution and the 1-0 design was negligible. It should be noted that all methods provide a somewhat different structure with the same amount of material, however the global topology in all cases was similar.

6.3 Curved cantilever with suspended mass

Another practical example where eigenfrequency optimization has significant potential, is that of suspended mass problems, where a structure is to be constructed to restrict or modify vibration characteristics of objects in space. Figure 17a shows the domain used for a curved cantilever with a single mass suspended at the tip, and part b of that figure shows the eigen modes and eigenfrequencies for the pre-optimized structure with an added mass ratio of 1.0. Note that the added mass ratio for this structure is defined as:

$$\frac{M_S}{\sum_{i=1}^{N_{el}} A_i \rho_i} \quad (32)$$

where M_S is the amount of added mass, divided by the mass of the continuum; therefore an added mass ratio of 1.0 signifies that a mass equal to the total structural mass is

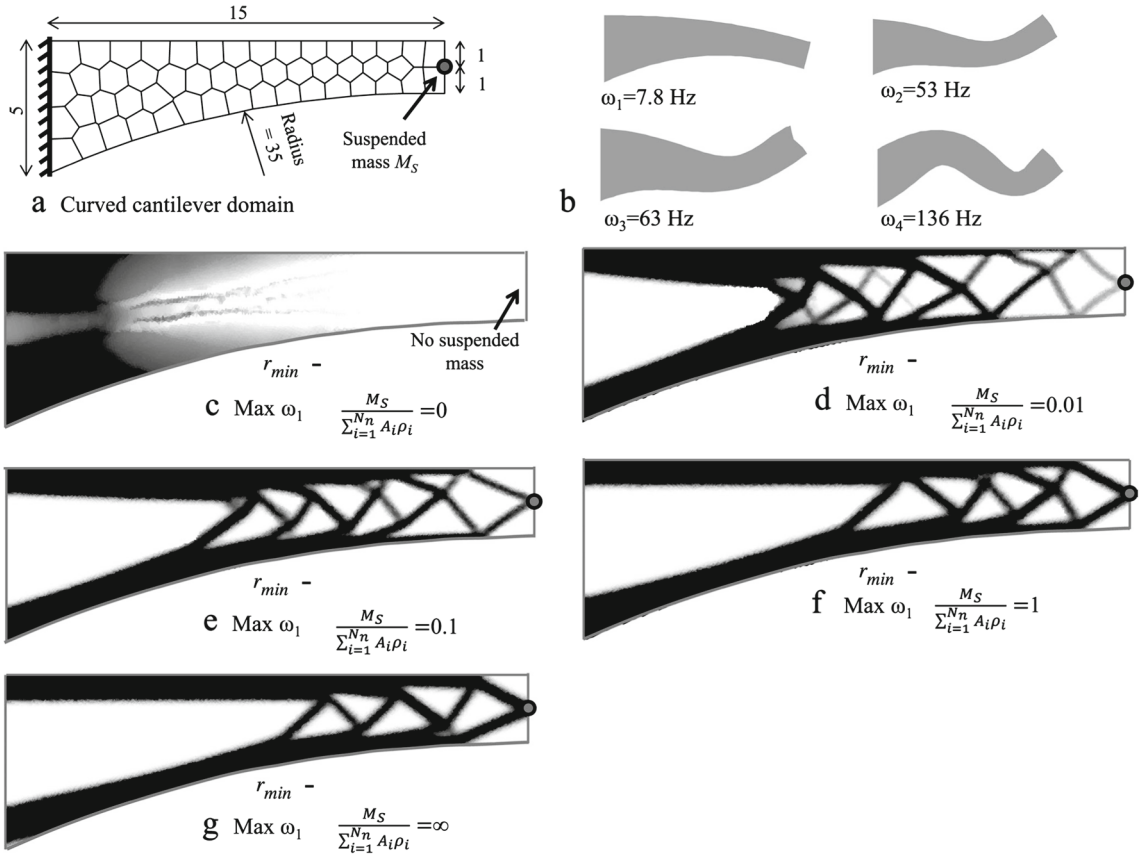

Fig. 17 **a** Geometry and boundary conditions for curved cantilever (representative mesh only, not used in analysis), **b** Initial mode shapes and eigenfrequencies for structure with 1.0 added mass ratio, **c** ω_1 maximized for structure with 0 added mass ratio, **d** ω_1 maximized for structure with 0.01 added mass ratio, **e** ω_1 maximized for structure with 0.1 added mass ratio, **f** ω_1 maximized for structure with 1.0 added mass ratio, **g** ω_1 maximized for structure with ∞ added mass ratio

suspended. The discretization adopted consists of 1,600 elements with a M4 MTOP approach and a minimum length scale of r_{min} = 0.25. The remainder of parameters for the structure and optimization are the same as those used for the simply supported beam case. When no mass is suspended at the tip of this structure, then most of the structural material moves towards the rigid support on the left where it can effectively be restrained from movement (Fig. 17c). Note

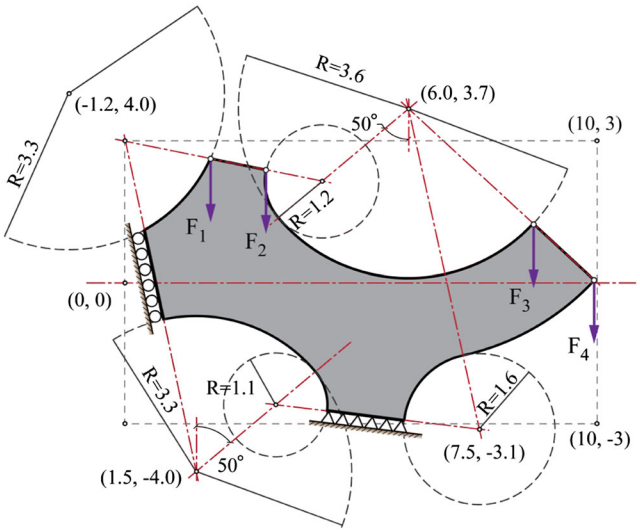

Fig. 18 Geometry of design domain and loading configuration

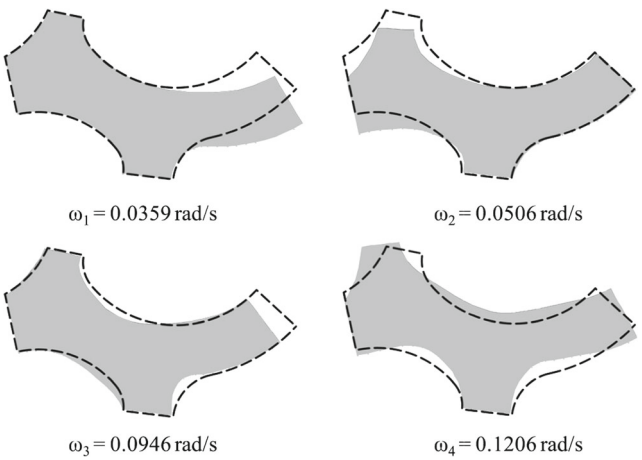

Fig. 19 Natural mode shapes and natural frequencies

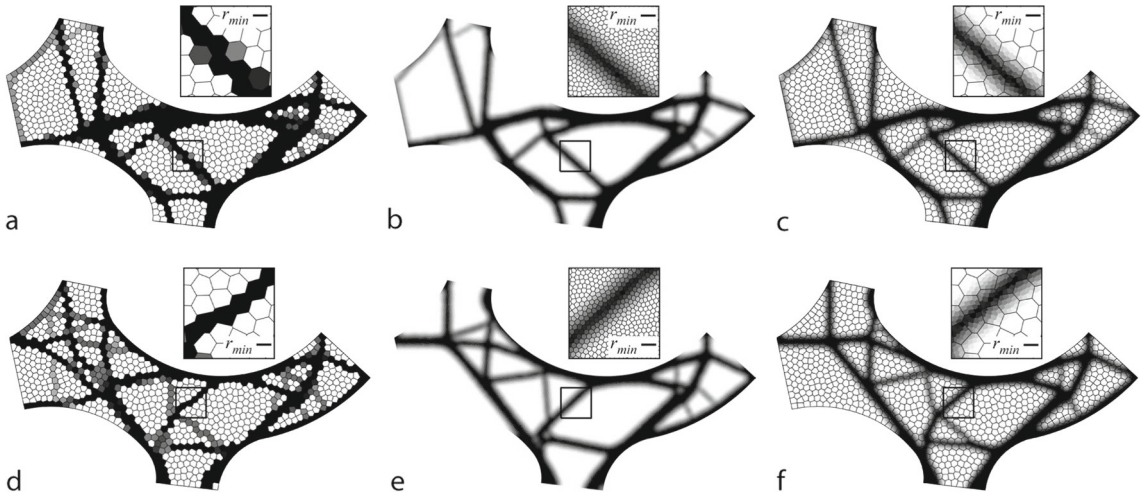

Fig. 20 Comparison of optimal topologies for multipoint forced vibration problem. Single load case: **a** 900 n-gons, **b** 13500 n-gons, **c** Pn/n15 approach, 900 n-gons, 13500 design variables. Multiple load cases: **d** 900 n-gons, **e** 13500 n-gons, **f** Pn/n15 approach, 900 n-gons, 13500 design variables

that since a minimum density is imposed, some material remains over the length of the cantilever. However, even for a small added mass ratio of 0.01, the structure forms a truss like system to restrict movement at the far tip of the beam. As the added mass ratio is increased, material moves from the support of the structure to other parts of the domain.

7 Forced vibration optimization example

A numerical example for minimization of the dynamic compliance is considered under harmonic excitations. The geometry of a curved structure is generated using PolyMesher (Talischi et al. 2012a) based on the parameters

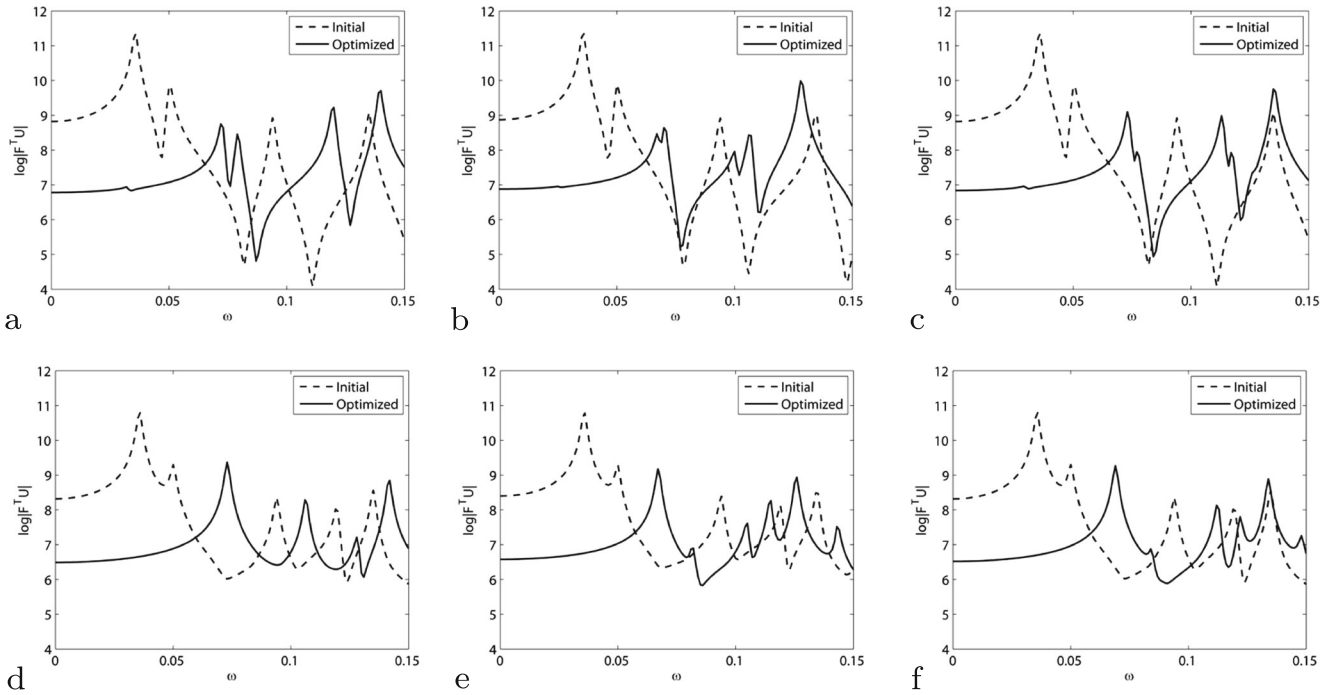

Fig. 21 The initial and optimized resonant response of the structures: Single load case: **a** 900 n-gons, **b** 13500 n-gons, **c** Pn/n15 approach, 900 n-gons, 13500 design variables. Multiple load cases: **d** 900 n-gons, **e** 13500 n-gons, **f** Pn/n15 approach, 900 n-gons, 13500 design variables

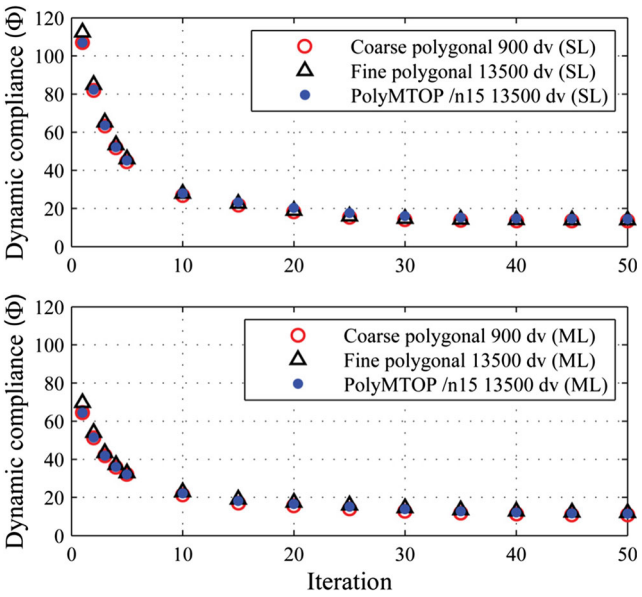

Fig. 22 Convergence history for optimization of dynamic compliance of multipoint excitation domain (dv = design/density variables, SL = single load case, ML = multiple load cases)

shown in Fig. 18. The structure is anchored at the bottom end and restrained in the horizontal direction at the left end. Harmonic excitations are applied at the arrows inscribed in Fig. 18. For the topology optimization, Young's modulus E, Poisson's ratio ν and initial density of the design variables ρ are set to $1N/m^2$, 0.3 and $1kg/m^3$, respectively. The volume fraction V_s is constrained to be 40 % of the design domain. The natural mode shapes and frequencies of the initial design domain which is the continuum domain completely filled with initial volume fraction are shown in Fig. 19.

The initial angular frequency of the forced vibration $\omega_s = 0.0$ and the final one $\omega_e = 0.015$ are set with the magnitude of force $\mathbf{F} = 1$, in (24). Two loading conditions such as a single load case where all four loads act simultaneously and multiple load cases where F_1, F_2, F_3 and F_4 represent each load case are considered for the optimization problem. For the multiple load cases, the optimization problem can be formulated as minimizing the sum of dynamic compliance induced by all loads. Therefore, the optimization problem considering multiple load cases can be stated as follows

$$\begin{aligned} &\min_{\rho} \quad \sum_{i=1}^{4} \int_{\omega_s}^{\omega_e} |\mathbf{F}_i^{\mathrm{T}} \mathbf{U}_i(\rho)| d\omega \\ &\text{s.t.} \quad V(\rho) = \int_{\Omega} \rho dV \leq V_s \end{aligned} \tag{33}$$

The design domain is discretized with 900 n-gons for both coarse and PolyMTOP analyses, and the projection function with a radius $r_{min} = 0.14$ is used. The penalization factors for the stiffness and mass are chosen as $p = 3$ and $q = 1$, respectively. The Method of Moving Asymptotes (MMA) (Svanberg 1987) is implemented in this example to solve the optimization problem for dynamic compliance.

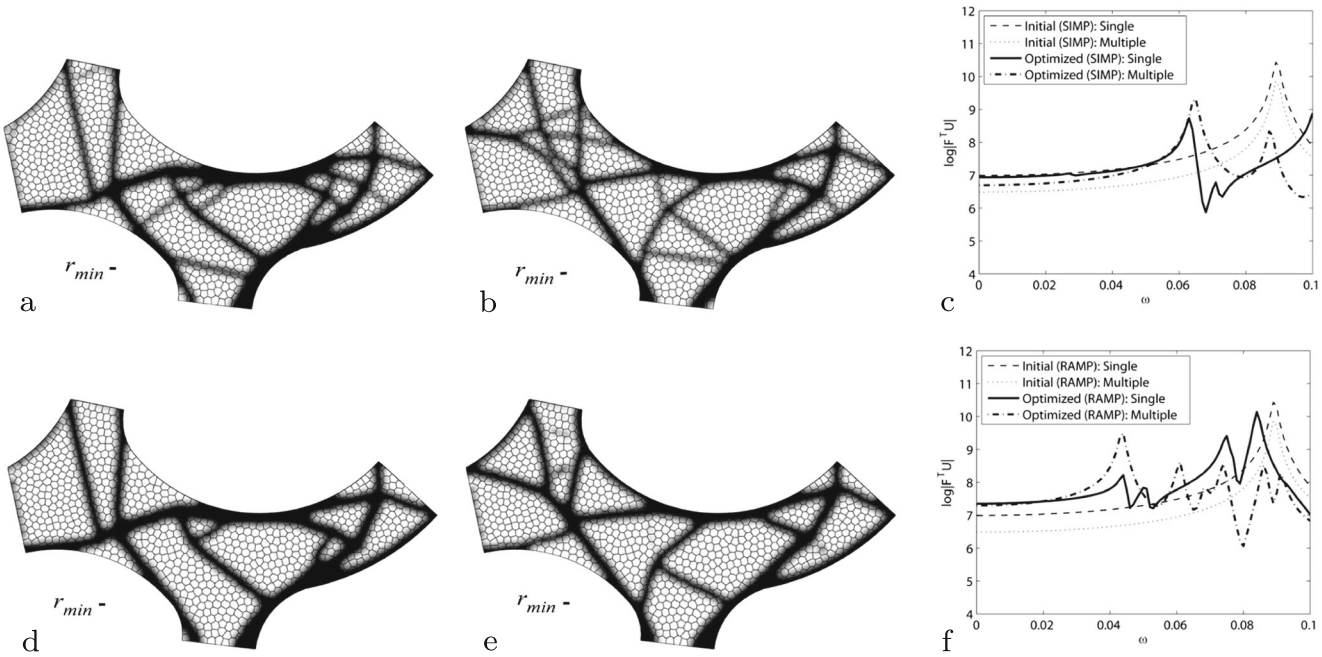

Fig. 23 Minimization of dynamic compliance. SIMP, continuation of $p(1-4)$: **a** Single load case, **b** Multiple load cases, **c** resonant response of the structures. RAMP, continuation of $s(0-64)$: **d** Single load case, **e** Multiple load cases, **f** resonant response of the structures

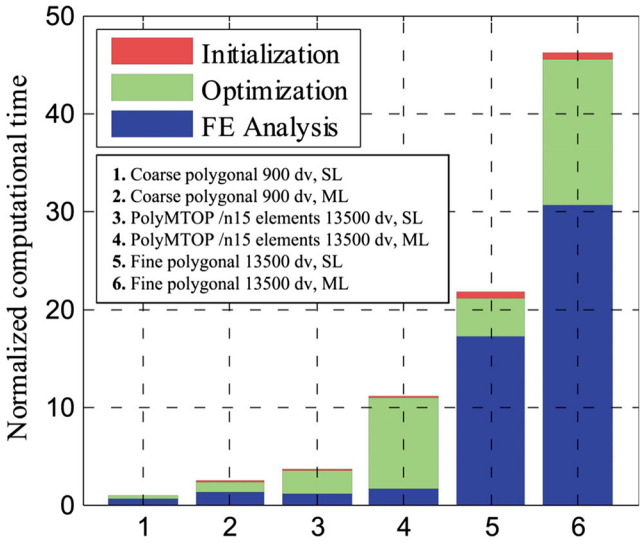

Fig. 24 Comparison of normalized computational times for optimization of forced vibration of multipoint excitation domain (dv = design/density variables, SL = single load case, ML = multiple load cases). Times are normalized with respect to the the SL coarse mesh computation (89 seconds in this case)

Coarse meshes with the optimal topology are presented in Fig. 20a and d (single and multiple load cases respectively), while parts c and f of that figure show the improved solutions through the use of the PolyMTOP approach. It is noted that the solution for the single load case is significantly different from the multiple load cases problem, particularly the material distributions on the left part of the design domain. Furthermore, a fine conventional mesh with 13,500 elements (Fig. 20b and e) is also optimized to verify the solution, and to compare the time improvement from the PolyMTOP scheme. For all cases, the dynamic response of the initial structure subject to periodic excitations is compared with the response of the optimized (Fig. 21). As can be seen from Fig. 21, the dynamic resonant response in the range of interest ($\omega_s = 0.0$ to $\omega_e = 0.015$) is significantly reduced for all cases through the optimization. While keeping the volume the same, the area underneath the dynamic response curve is reduced (Fig. 21), and there is improved dynamic behavior for both the single and multiple load cases. The optimal designs are similar for the coarse, the fine, and the MTOP meshes, however the dynamic resonance, although similar is not identical after the optimization. The difference in the higher frequency response (i.e. above $\omega = 0.03$) can be attributed to the different performance of the FE analysis for each method as discussed in Section 2.4. Finally, the convergence results of the dynamic compliance for the six cases are shown in Fig. 22.

Furthermore, topology optimization for the dynamic compliance problem was carried out using the SIMP and RAMP continuation schemes described for the fixed ends arch structure (Section 6.2). 900 n-gon meshes identical to the previous example were implemented for this problem in order to investigate the influence of the SIMP, RAMP, and the continuation approach on optimal topologies. Figure 23 shows optimal topologies for the single and multiple loads cases with both the SIMP and RAMP schemes using the continuation approach. Based on results of part *c* and part *f* in Fig. 20 and results of part *a* and *b* in Fig. 23, one can notice that the continuation of the penalization factor has affected the optimal solutions, especially in the scenario with multiple load cases. Moreover, different topologies were obtained with each SIMP and RAMP scheme as shown in Fig. 23. Although the topologies are different for these cases, the optimal dynamic response for all cases is somewhat similar. Note that in the continuation cases the optimized response is not necessarily lower than that of the initial configuration, since a different penalization factor is used in each case. Again, the compliance converges in the same manner for all methods. Finally, Fig. 24 shows the normalized computational time of the cases in Fig. 20 for 50 iterations of the optimization scheme. It can be noted that using a fine mesh in PolyTOP alone is about four times more expensive than using the PolyMTOP method with less finite elements and a similar number of density, and design variables.

8 Concluding remarks

This paper introduces a method for combining a coarse finite element mesh with finer design and density meshes to obtain high quality optimization solutions for a reduced computational cost. Polygonal elements presented in recently published PolyTOP software are shown to approximate dynamic behaviors better than other conventional elements, and are thereby used as the focus for this study. Two approaches using either matching or non-matching sub-discretizations are investigated to split up the polygonal elements in order to facilitate the multiresolution analysis. The computational approach is shown to be particularly beneficial for structural dynamics problems such as eigenfrequency and forced vibration optimization, since these problems require substantial time in finite element analysis. The multiresolution approach produces solutions with high resolution through an increase in the time required for optimizing the design variables, however, the approach can use a smaller number of elements and nodes, and can thereby avoid increasing the costlier finite element calculations. Several examples of the polygonal multiresolution topology optimization are shown for static as well as dynamic cases. These include: a curved beam domain, a simply supported beam, an arch structure, and a cantilever beam with

suspended mass. The results show that the algorithm is effective at producing high resolution results suitable for efficient and computationally effective structural design. The efficient scheme for optimization of structures with dynamic loads could be useful in civil, mechanical, and aerospace engineering applications where the structural dynamic properties need to be controlled. The concepts shown herein could further be extended to acoustic and wave propagation problems where eigenfrequency response needs to be controlled.

Acknowledgments The authors gratefully acknowledge funding provided by the National Science Foundation (NSF) through projects CMMI 1234243 and CMMI 1321661. The first author is thankful for support from the NSF Graduate Research Fellowship Program. We also acknowledge support from the Donald B. and Elizabeth M. Willett endowment at the University of Illinois at Urbana-Champaign. The fourth author acknowledges the support by the SNU Invitation Program for Distinguished Scholars and the Integrated Research Institute of Construction and Environmental Engineering at Seoul National University. Any opinion, finding, conclusions or recommendations expressed here are those of the authors and do not necessarily reflect the views of the sponsors.

Nomenclature

n number of density elements in the displacement element
$\mathbf{K}$ global stiffness matrix
$\mathbf{K}_e$ stiffness matrix of displacement element e
N_{el} number of elements in mesh
$\mathbf{D}$ constitutive matrix
$\mathbf{B}$ strain-displacement matrix of shape function derivatives
$\mathbf{x}$ position of a point in the domain, coordinate vector
E Young's modulus
E^0 Young's modulus of solid material
ρ density values determined based on position in domain ($\mathbf{x}$)
p stiffness penalization parameter
$\mathbf{M}$ global mass matrix
$\mathbf{M}_e$ mass matrix of displacement element e
$\mathbf{N}^e$ shape functions of element e
q mass penalization parameter
C static compliance
$\mathbf{u}$ global displacement vector
$\mathbf{f}$ global force vector
$\mathbf{d}$ vector of design variables
V_s prescribed volume
λ_j j_{th} eigenvalue of structure
ω_j j_{th} eigenfrequency of structure
ϕ_j j_{th} eigenvector of structure
d_n design variable n
β bound parameter for optimization
$\mathbf{C}$ global damping matrix
Φ dynamic compliance
ω_s initial angular frequency of external forces
ω_e final angular frequency of external forces
r_{min} minimum length scale parameter
w weight function for linear projection
M_S suspended mass

Appendix: Sensitivity analysis

To optimize for the objectives defined in Section 3, it is necessary that we calculate the sensitivity of the objective functions, and constraints with respect to the density variables. Since these are composed of the stiffness and mass terms, we calculate the derivatives of $\mathbf{K}_e$ and $\mathbf{M}_e$ as:

$$\frac{\partial \mathbf{K}_e}{\partial d_n} = \frac{\partial \mathbf{K}_e}{\partial \rho_i}\frac{\partial \rho_i}{\partial d_n} = \frac{\partial \left(\sum_{j=1}^{N_n} (\rho_j)^p \mathbf{I}_j\right)}{\partial \rho_i}\frac{\partial \rho_i}{\partial d_n} = (\rho_i)^{p-1}\mathbf{I}_i \frac{\partial \rho_i}{\partial d_n} \tag{34}$$

and

$$\frac{\partial \mathbf{M}_e}{\partial d_n} = \frac{\partial \mathbf{M}_e}{\partial \rho_i}\frac{\partial \rho_i}{\partial d_n} = \frac{\partial \left(\sum_{j=1}^{N_n} (\rho_j)^q \mathbf{H}_j\right)}{\partial \rho_i}\frac{\partial \rho_i}{\partial d_n} = (\rho_i)^{p-1}\mathbf{H}_i \frac{\partial \rho_i}{\partial d_n} \tag{35}$$

The sensitivity for the volume constraint can similarly be calculated as

$$\frac{\partial V}{\partial d_n} = \frac{\partial V}{\partial \rho_i}\frac{\partial \rho_i}{\partial d_n} \tag{36}$$

Note that the calculation of the sensitivity of the density variables with respect to design variables ($\partial \rho_i / \partial d_n$) is presented in Section 3.4. Subsequently, the sensitivity of static compliance can be calculated from the element displacement $\mathbf{u}_e$ as:

$$\frac{\partial C}{\partial d_n} = -\mathbf{u}_e \frac{\partial \mathbf{K}_e}{\partial d_n}\mathbf{u}_e \tag{37}$$

A.1 Sensitivity analysis of eigenfrequencies

For free body vibrations the sensitivity of the fundamental eigenvalue λ for a specific element can be calculated as:

$$\frac{\partial \lambda_j}{\partial d_n} = -\phi_{je}^T \left(\frac{\partial \mathbf{K}_e}{\partial d_n} - \lambda_j \frac{\partial \mathbf{M}_e}{\partial d_n}\right)\phi_{je} \tag{38}$$

where ϕ_{je} is the eigenvector map for element e (Haftka and Adelman 1989). Furthermore the sensitivity of the first eigenvector for the entire structure can be re-written in vector form as:

$$\nabla \lambda_j = \left\{\phi_j^T \left(\frac{\partial \mathbf{K}}{\partial d_1} - \lambda_j \frac{\partial \mathbf{M}}{\partial d_1}\right)\phi_j, \ldots, \phi_j^T \left(\frac{\partial \mathbf{K}}{\partial d_{N_{des}}} - \lambda_j \frac{\partial \mathbf{M}}{\partial d_{N_{des}}}\right)\phi_j\right\} \tag{39}$$

Alternatively, Pedersen and Pedersen (2013) have introduced eigenfrequency sensitivities based on local subdomains. However, in the case where there are N multiple eigenfrequencies (Seyranian et al. 1994), the following generalized gradient can be used in the optimization:

$$\mathbf{f}_{sk} = \left\{ \phi_s^T \left(\frac{\partial \mathbf{K}}{\partial d_1} - \lambda \frac{\partial \mathbf{M}}{\partial d_1} \right) \phi_k, \right. \\ \left. ..., \phi_s^T \left(\frac{\partial \mathbf{K}}{\partial d_{N_{des}}} - \lambda_j \frac{\partial \mathbf{M}}{\partial d_{N_{des}}} \right) \phi_k \right\} \\ s, k = n, ..., n + N - 1. \tag{40}$$

A.2 Sensitivity analysis of the dynamic compliance

Sensitivity analysis for the dynamic compliance in (24) with respect to a design variable d_n is derived by a chain rule for mathematical programming:

$$\frac{\partial \Phi}{\partial d_n} = \sum_{\rho_i} \frac{\partial \Phi}{\partial \rho_i} \frac{\partial \rho_i}{\partial d_n} \tag{41}$$

The derivatives of $\partial \Phi / \partial \rho_i$ can be obtained as follows

$$\frac{\partial \Phi}{\partial \rho_i} = \begin{pmatrix} \nabla \mathbf{U}_\mathrm{R} \Phi \\ \nabla \mathbf{U}_\mathrm{I} \Phi \end{pmatrix}^\mathrm{T} \begin{pmatrix} \nabla \rho_i \mathbf{U}_\mathrm{R} \\ \nabla \rho_i \mathbf{U}_\mathrm{I} \end{pmatrix} \tag{42}$$

where

$$\begin{pmatrix} \nabla \rho_i \mathbf{U_R} \\ \nabla \rho_i \mathbf{U_I} \end{pmatrix} = - \begin{bmatrix} \mathbf{K} - \omega^2 \mathbf{M} & -\omega \mathbf{C} \\ \omega \mathbf{C} & \mathbf{K} - \omega^2 \mathbf{M} \end{bmatrix}^{-1} \\ \times \frac{\partial}{\partial \rho_i} \begin{bmatrix} \mathbf{K} - \omega^2 \mathbf{M} & -\omega \mathbf{C} \\ \omega \mathbf{C} & \mathbf{K} - \omega^2 \mathbf{M} \end{bmatrix} \begin{pmatrix} \mathbf{U}_\mathrm{R} \\ \mathbf{U}_\mathrm{I} \end{pmatrix} \tag{43}$$

Equation (43) is obtained from derivatives of (20). It is assumed that $\mathbf{F}_\mathrm{R}$ and $\mathbf{F}_\mathrm{I}$ are independent from the filtered density. The term in the first parentheses of (42) is used as

$$\begin{pmatrix} \boldsymbol{\lambda}_\mathrm{R} \\ \boldsymbol{\lambda}_\mathrm{I} \end{pmatrix} = \begin{bmatrix} \mathbf{K} - \omega^2 \mathbf{M} & -\omega \mathbf{C} \\ \omega \mathbf{C} & \mathbf{K} - \omega^2 \mathbf{M} \end{bmatrix}^{-\mathrm{T}} \begin{pmatrix} \nabla \mathbf{U}_\mathrm{R} \Phi \\ \nabla \mathbf{U}_\mathrm{I} \Phi \end{pmatrix} \tag{44}$$

where $\nabla \mathbf{U}_\mathrm{R} \Phi$ and $\nabla \mathbf{U}_\mathrm{I} \Phi$ are the gradients of Φ with respect to $\mathbf{U}_\mathrm{R}$ and $\mathbf{U}_\mathrm{I}$, respectively. Those gradients can be computed as

$$\nabla \mathbf{U}_\mathrm{R} \Phi = \frac{(\mathbf{F}_\mathrm{R}^\mathrm{T} \mathbf{U}_\mathrm{R} - \mathbf{F}_\mathrm{I}^\mathrm{T} \mathbf{U}_\mathrm{I}) \mathbf{F}_\mathrm{R}}{\Phi} \\ + \frac{(\mathbf{F}_\mathrm{R}^\mathrm{T} \mathbf{U}_\mathrm{I} + \mathbf{F}_\mathrm{I}^\mathrm{T} \mathbf{U}_\mathrm{R}) \mathbf{F}_\mathrm{I}}{\Phi} \\ \nabla \mathbf{U}_\mathrm{I} \Phi = \frac{(-\mathbf{F}_\mathrm{R}^\mathrm{T} \mathbf{U}_\mathrm{R} + \mathbf{F}_\mathrm{I}^\mathrm{T} \mathbf{U}_\mathrm{I}) \mathbf{F}_\mathrm{I}}{\Phi} \\ + \frac{(\mathbf{F}_\mathrm{R}^\mathrm{T} \mathbf{U}_\mathrm{I} + \mathbf{F}_\mathrm{I}^\mathrm{T} \mathbf{U}_\mathrm{R}) \mathbf{F}_\mathrm{R}}{\Phi} \tag{45}$$

Similar to (19), let $\boldsymbol{\lambda} = \boldsymbol{\lambda}_\mathrm{R} + i\boldsymbol{\lambda}_\mathrm{I}$, $\nabla \mathbf{U} \Phi = \nabla \mathbf{U}_{\mathrm{R}\Phi} + i \nabla \mathbf{U}_{\mathrm{I}\Phi}$ and assume $\mathbf{M}$, $\mathbf{C}$ and $\mathbf{K}$ are symmetric. The complex vector form of (45) can be described as

$$\nabla \mathbf{U} \Phi = \frac{\mathbf{F}^\mathrm{T} \mathbf{U}}{\Phi} \bar{\mathbf{F}} \tag{46}$$

where $\bar{\mathbf{F}}$ denotes the complex conjugate of $\mathbf{F}$. Then (44) can be expressed in complex form as:

$$[\mathbf{K} + i\omega \mathbf{C} - \omega^2 \mathbf{M}] \bar{\boldsymbol{\lambda}} = \overline{\nabla \mathbf{U} \Phi} = \frac{\bar{\mathbf{F}}^T \bar{\mathbf{U}}}{\Phi} \mathbf{F} \tag{47}$$

where $\bar{\boldsymbol{\lambda}}$ and $\overline{\nabla \mathbf{U} \Phi}$ denote the complex conjugate of $\boldsymbol{\lambda}$ and $\nabla \mathbf{U} \Phi$, respectively. For the linear system, one can show that the solution of (47) in terms of $\bar{\boldsymbol{\lambda}}$ is proportional to one of (20) in terms of $\mathbf{U}$. Therefore, the conjugate of $\bar{\boldsymbol{\lambda}}$ can be computed by a scalar factor, that is

$$\bar{\boldsymbol{\lambda}} = \frac{\bar{\mathbf{F}}^\mathrm{T} \bar{\mathbf{U}}}{\Phi} \mathbf{U} \tag{48}$$

Finally, substitution of (44) and (48) into (42) yields the following

$$\frac{\partial \Phi}{\partial \rho_i} = - \begin{pmatrix} \boldsymbol{\lambda}_\mathrm{R} \\ \boldsymbol{\lambda}_\mathrm{I} \end{pmatrix}^\mathrm{T} \frac{\partial}{\partial \rho_i} \begin{bmatrix} \mathbf{K} - \omega^2 \mathbf{M} & -\omega \mathbf{C} \\ \omega \mathbf{C} & \mathbf{K} - \omega^2 \mathbf{M} \end{bmatrix} \begin{pmatrix} \mathbf{U}_\mathrm{R} \\ \mathbf{U}_\mathrm{I} \end{pmatrix} \tag{49}$$

$$\frac{\partial \Phi}{\partial \rho_i} = -Re \left\{ \frac{\bar{\mathbf{F}}^\mathrm{T} \bar{\mathbf{U}}}{\Phi} \mathbf{U}^\mathrm{T} \frac{\partial (\mathbf{K} + i\omega C - \omega^2 M)}{\partial \rho_i} \mathbf{U} \right\} \\ = -Re \left\{ \boldsymbol{\lambda}^* \frac{\partial (\mathbf{K} + i\omega C - \omega^2 M)}{\partial \rho_i} \mathbf{U} \right\} \tag{50}$$

where $\boldsymbol{\lambda}^*$ is a Hermitian transpose of $\boldsymbol{\lambda}$. That is $\boldsymbol{\lambda}^* := \bar{\boldsymbol{\lambda}}^\mathrm{T}$

References

Almeida SRM, Paulino GH, Silva ECN (2009) A simple and effective inverse projection scheme for void distribution control in topology optimization. Struct Multidiscip Optim 39(4):359–371

Bendsøe MP (1989) Optimal shape design as a material distribution problem. Struct Optim 1(4):193–202

Bendsøe MP, Sigmund O (2004) Topology optimization: Theory and methods and applications. Springer

Bendsøe MP, Olhoff N, Taylor JE (1983) A variational formulation for multicriteria structural optimization. J Struct Mech 11(4):523–544

Bourdin B (2001) Filters in topology optimization. Int J Numer Methods Eng 50(9):2143–2158

Bratus A, Seiranian A (1983) Bimodal solutions in eigenvalue optimization problems. J Appl Math Mech 47(4):451–457

Cook R, Malkus D, Plesha M, Witt R (2007) Concepts and applications of finite element analysis, 4th edn. Wiley

Dahl J, Jensen JS, Sigmund O (2007) Topology optimization for transient wave propagation problems in one dimension. Struct Multidiscip Optim 36(6):585–595

Díaz A, Sigmund O (1995) Checkerboard patterns in layout optimization. Struct Optim 10(1):40–45

Du J, Olhoff N (2007) Topological design of freely vibrating continuum structures for maximum values of simple and multiple eigenfrequencies and frequency gaps. Struct Multidiscip Optim 34(2):91–110

Ghosh S (2011) Micromechanical analysis and multi-scale modeling using the Voronoi cell finite element method (computational mechanics and applied analysis). CRC Press

Guest JK (2009) Imposing maximum length scale in topology optimization. Struct Multidiscip Optim 37(5):463–473

Guest JK, Prévost JH, Belytschko T (2004) Achieving minimum length scale in topology optimization using nodal design variables and projection functions. Int J Numer Methods Eng 61(2): 238–254

Haftka RT, Adelman HM (1989) Recent developments in structural sensitivity analysis. Struct Optim 1(3):137–151

Huang X, Zuo Z, Xie Y (2010) Evolutionary topological optimization of vibrating continuum structures for natural frequencies. Comput Struct 88(5–6):357–364

Jensen JS (2007) Topology optimization of dynamics problems with Padé approximants. Int J Numer Methods Eng 72(13):1605–1630

Jog C (2002) Topology design of structures subjected to periodic loading. J Sound Vib 253(3):687–709

Jog CS, Haber RB (1996) Stability of finite element models for distributed-parameter optimization and topology design. Comput Methods Appl Mech Eng 130(3):203–226

Larsen AA, Laksafoss B, Jensen JS, Sigmund O (2008) Topological material layout in plates for vibration suppression and wave propagation control. Struct Multidiscip Optim 37(6):585–594

Ma ZD, Kikuchi N, Cheng HC (1995) Topological design for vibrating structures. Comput Methods Appl Mech Eng 121(1–4):259–280

Masur E (1985) Some additional comments on optimal structural design under multiple eigenvalue constraints. Int J Solids Struct 21(2):117–120

Matsui K, Terada K (2004) Continuous approximation of material distribution for topology optimization. Int J Numer Methods Eng 59(14):1925–1944

Maute K, Allen M (2004) Conceptual design of aeroelastic structures by topology optimization. Struct Multidiscip Optim 27(1–2):27–42

Mijar A, Swan C, Arora J, Kosaka I (1998) Continuum topology optimization for concept design of frame bracing systems. J Struct Eng 129(12):1707–1716

Nguyen TH, Paulino GH, Song J, Le CH (2009) A computational paradigm for multiresolution topology optimization (MTOP). Struct Multidiscip Optim 41(4):525–539

Nguyen TH, Paulino GH, Song J, Le CH (2012) Improving multiresolution topology optimization via multiple discretizations. Int J Numer Methods Eng 92(6):507–530

Nguyen TH, Le CH, Hajjar JF (2013) High-order finite elements for topology optimization. In: 10th World congress on structural and multidisciplinary optimization. Orlando

Olhoff N (1976) Optimization of vibrating beams with respect to higher order natural frequencies. J Struct Mech 4(1):87–122

Olhoff N (1989) Multicriterion structural optimization via bound formulation and mathematical programming. Struct Optim 1(1):11–17

Olhoff N, Niu B, Cheng G (2012) Optimum design of band-gap beam structures. Int J Solids Struct 49(22):3158–3169

Parvizian J, Düster A, Rank E (2011) Topology optimization using the finite cell method. Optim Eng 13(1):57–78

Paulino GH, Le CH (2008) A modified Q4/Q4 element for topology optimization. Struct Multidiscip Optim 37(3):255–264

Pedersen P, Pedersen NL (2013) A note on eigenfrequency sensitivities and structural eigenfrequency optimization based on local sub-domain frequencies. Struct Multidiscip Optim

Petersson J, Sigmund O (1998) Slope constrained topology optimization. Int J Numer Methods Eng 41(8):1417–1434

Rahmatalla S, Swan C (2004) A Q4/Q4 continuum structural topology optimization implementation. Struct Multidiscip Optim 27 (1–2):130–135

Rozvany GIN, Zhou M, Birker T (1992) Generalized shape optimization without homogenization. Struct Optim 4(3–4):250–252

Seyranian AP, Lund E, Olhoff N (1994) Multiple eigenvalues in structural optimization problems. Struct Optim 8(4):207–227

Sigmund O, Petersson J (1998) Numerical instabilities in topology optimization: a survey on procedures dealing with checkerboards, mesh-dependencies and local minima. Struct Optim 16 (1):68–75

Sleesongsom S, Bureerat S (2013) New conceptual design of aeroelastic wing structures by multi-objective optimization. Eng Optim 45(1):107–122

Stolpe M, Svanberg K (2001) An alternative interpolation scheme for minimum compliance topology optimization. Struct Multidiscip Optim 22(2):116–124

Stromberg LL, Beghini A, Baker WF, Paulino GH (2011) Application of layout and topology optimization using pattern gradation for the conceptual design of buildings. Struct Multidisc Optim 43(2):165–180

Sukumar N (2004) Construction of polygonal interpolants: a maximum entropy approach. Int J Numer Methods Eng 61(12):2159–2181

Sukumar N, Malsch EA (2006) Recent advances in the construction of polygonal finite element interpolants. Archives Comput Methods Eng 13(1):129–163

Sutradhar A, Paulino GH, Miller MJ, Nguyen TH (2010) Topological optimization for designing patient-specific large craniofacial segmental bone replacements. Proc Natl Acad Sci US A 107(30):13,222–7

Svanberg K (1987) The method of moving asymptotesa new method for structural optimization. Int J Numer Methods Eng 24(2):359–373

Talischi C, Paulino GH, Le CH (2009a) Honeycomb Wachspress finite elements for structural topology optimization. Struct Multidiscip Optim 37(6):569–583

Talischi C, Paulino GH, Pereira A, Menezes IFM (2009b) Polygonal finite elements for topology optimization: a unifying paradigm. Int J Numer Methods Eng 82(6):671–698

Talischi C, Paulino GH, Pereira A, Menezes IFM (2012a) PolyMesher: a general-purpose mesh generator for polygonal elements written in MATLAB. Struct Multidiscip Optim 45(3): 309–328

Talischi C, Paulino GH, Pereira A, Menezes IFM (2012b) PolyTop: a MATLAB implementation of a general topology optimization framework using unstructured polygonal finite element meshes. Struct Multidiscip Optim 45(3):329–357

Taylor J, Bendsøe MP (1984) An interpretation for min-max structural design problems including a method for relaxing constraints. Int J Solids Struct 20(4):301–314

Tcherniak D (2002) Topology optimization of resonating structures using SIMP method. Int J Numer Methods Eng 54(11):1605–1622

Tsai TD, Cheng CC (2013) Structural design for desired eigenfrequencies and mode shapes using topology optimization. Struct Multidiscip Optim 47(5):673–686

Wang F, Lazarov BS, Sigmund O (2010) On projection methods, convergence and robust formulations in topology optimization. Struct Multidiscip Optim 43(6):767–784

Yang RJ, Chahande AI (1995) Automotive applications of topology optimization. Struct Optim 9(3–4):245–249

Yoon GH (2010a) Maximizing the fundamental eigenfrequency of geometrically nonlinear structures by topology optimization based on element connectivity parameterization. Comput Struct 88 (1–2):120–133

Yoon GH (2010b) Structural topology optimization for frequency response problem using model reduction schemes. Comput Methods Appl Mech Eng 199(25–28):1744–1763

Zhou K (2013) Topology optimization of truss-like continuum structures for natural frequencies. Struct Multidiscip Optim 47(4):613–619